International Journal of Hydrogen Energy 102 (2025) 1507–1529

Contents lists available at ScienceDirect

International Journal of Hydrogen Energy

journal homepage: www.elsevier.com/locate/he

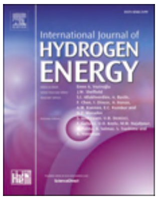

Overview of gaseous hydrogen-assisted fatigue crack growth in ferritic iron and steels: Bridging micro and macro

Yuhei Ogawa [a,*], Osamu Takakuwa [b], Akinobu Shibata [a]

[a] Research Center for Structural Materials, National Institute for Materials Science (NIMS), 1-2-1 Sengen, Tsukuba, 305-0047, Japan
[b] Department of Mechanical Engineering, Kyushu University, 744 Motooka, Nishi-ku, Fukuoka, 819-0395, Japan

ARTICLE INFO

Handling Editor: Søren Juhl Andreasen

Keywords:
Hydrogen embrittlement
Fatigue crack growth
Ferritic steels
Hydrogen gas

ABSTRACT

Acceleration of fatigue crack growth in steels under hydrogenating environments (hydrogen-assisted fatigue crack growth, HA-FCG) is of critical concern for the defect-tolerant engineering design of pressure vessels and pipelines for the storage and transportation of gaseous hydrogen. This overview provides a state-of-the-art understanding of the HA-FCG in ferrite-based materials with a primary basis on the authors' recent works. The influences of gas pressure, temperature, stress intensity, and loading frequency are summarized, focusing on two representative failure modes: intergranular (IG); and cleavage-involving transgranular (CIT). The latter one has conventionally been termed quasi-cleavage (QC). Crack path crystallography and deformation microstructures beneath these IG and CIT are provided as supplemental information to figure out the underlying fracture mechanisms. Comprehensive models accounting for the HA-FCG in ferrite are finally established. Our models construct new bridges between microscale fracture behaviors and macroscale dependencies of the FCG acceleration on environmental and mechanistic variables.

1. Introduction

As an energy carrier with the potential to resolve escalating petroleum exhaustion and environmental problems, hydrogen (H or H_2) is one of the renovative candidates for the forthcoming establishment of sustainable development goals and carbon neutrality [1–5]. Since the 2000s, an obstacle to the widespread utilization of H has been to expand the infrastructures and platforms that enable a seamless energy supply. The most promising way to store and transport H is to handle it as pressurized gaseous H_2 or liquid H_2 [6–8]. However, when the metal components constituting the infrastructures are directly in contact with H_2 gas, H_2 molecules dissociate into H atoms on the metal surface and subsequently dissolve into the crystal lattice. Accordingly, degradation of the material's mechanical properties, *i.e.*, hydrogen embrittlement (HE) [9–12], is a serious concern, a phenomenon first discovered in an old paper by Johnson in 1874 [13].

In H-related infrastructures such as H_2 refueling stations for fuel cell vehicles, low-alloyed carbon steels with body-centered cubic (BCC) structures are primary constituents for the storage cylinder of pressurized H_2 gas [14–17]. Moreover, it is under consideration in Europe and the United States that the natural gas pipelines, also made of carbon steel, are diverted into long-distance H_2 gas transport [18–21]. Although low-alloyed carbon steels have a non-substitutable advantage in terms of economic efficiency, their HE-susceptibility is severe compared with highly alloyed austenitic steels with stable face-centered cubic (FCC) structure [22–26]. The detrimental influences of H in BCC iron and low-alloyed carbon steels manifest as decreases in tensile strength [25,27,28], fracture toughness [26,29–31], static crack growth threshold [29,32,33], and fatigue life [34–36]. These can be attributed to a higher mobility of H atoms through the BCC lattice than that in FCC [23,37–39], arrowing their rapid accumulation into potential fracture nucleation sites [40]. In particular, acceleration of fracture is crucial for the propagation of fatigue cracks [20,26,41–46], once the cracks are generated at stress concentration sites or material surfaces. The fatigue crack growth (FCG) rate is of significant importance for pressure vessels and pipelines because these components are subjected to cyclic loading due to the fluctuation of internal gas pressure. Thus, a reliable method of defect-tolerant design and the development of innovative steels that take the H-assisted (HA-) FCG into account and suppress/control it are desired.

A notable aspect of BCC carbon steels is the diversity in their internal microstructures. Depending on thermal histories during their casting

---

* Corresponding author.
E-mail address: OGAWA.Yuhei@nims.go.jp (Y. Ogawa).

https://doi.org/10.1016/j.ijhydene.2025.01.136
Received 18 October 2024; Received in revised form 7 January 2025; Accepted 9 January 2025

and processing, the material exhibits either ferrite, pearlite, martensite, and bainite or aggregate of them. Accordingly, the materials display a wide range of strength levels and various combinations of superior/inferior mechanical properties [47,48]. Under the absence of environmental effects, the FCG in a stable Stage II regime (Fig. 1(a) and (b)) is insensitive to the microstructure nor yield/tensile strength of the materials [46,49–51]. Therefore, the microstructural influences on FCG have often not been discussed. However, once H is involved, such a microstructure-insensitive property notably changes to microstructure-sensitive [46,52–57], making us securely select the compatible materials for H-related infrastructures. Nevertheless, such a microstructure-susceptible nature of HA-FCG conversely implies that the magnitude of FCG acceleration can more or less be controlled/suppressed by optimizing the steel microstructures *via* adequate thermo-mechanical processing without relying on expensive alloying elements.

Since the late 1970s, pieces of knowledge on HA-FCG have been built up mainly on ferritic [42,44,45,53,59,60] and martensitic [15,56,61–65] steels in H_2 gas and other hydrogenating corrosive environments. The scope has recently been extended to pearlitic steel [46,54], which exhibits superior HA-FCG resistance than the former two steel types. Table 1 lists the available literature regarding the HA-FCG in ferritic iron and steels in H_2 gas with information on examined materials and testing conditions. The number of publications has particularly increased since the 2010s, accompanying an escalating severity of environmental gas pressure used for the experiments. However, the understanding of the intrinsic mechanisms responsible for the crack growth acceleration, their correlation with each microstructural constituent, and fracture behaviors are far from complete. Toward the selection and design of robust H-compatible steels, which may have complex multimodal microstructures, we should first obtain a more comprehensive understanding of the elementary processes of HA-FCG in the above-noted four conventional microstructures in their single-phase state. This paper specifically focuses on the simplest one, ferrite, reviewing the related key experimental findings. It is a longstanding principle that HE in structural steels becomes more pronounced as their strength level increases in static loading conditions, *i.e.*, tensile and delayed-fracture tests [25,26,29,32]. Nevertheless, HA-FCG is still serious even in low-to-moderate-strength ferritic materials with yield stresses of merely ~400 MPa [42,44,45,59], motivating the researchers' responsibility toward more in-depth investigations.

In attempting to enhance our understanding of the fracture phenomena by simplifying the microstructure, the authors' group has conducted a series of studies on high-purity polycrystalline iron as a model system of ferritic materials [74,76–79]. This review is based primarily on our knowledge of pure iron, summarizing its HA-FCG characteristics and influences of mechanistic (*e.g.*, stress intensity, load ratio, and loading frequency) as well as environmental (*e.g.*, H_2 gas pressure, temperature, and purity) variables. Data from other commercial ferrite-based steels are also included. The underlying mechanisms that can consistently rationalize the overall experimental findings are discussed by combining the macroscopic FCG behavior with fractography and deformation substructures beneath the fracture surface. Finally, the current status of unresolved issues that should be tackled in the future will be highlighted.

2. Macroscale phenomenology

2.1. Crack propagation stages

The FCG properties in metallic materials are generally evaluated on a double-logarithmic diagram, where crack propagation distance per loading cycle (crack growth rate), da/dN, is plotted against the stress intensity factor range, ΔK: da/dN-ΔK curve. The loading is usually done in a sinusoidal waveform with a positive load ratio, $R = P_{min}/P_{max}$, where P_{min} and P_{max} are the minimum and maximum loads during the test (Fig. 1 (c)). Several suitable specimen types for the FCG test are

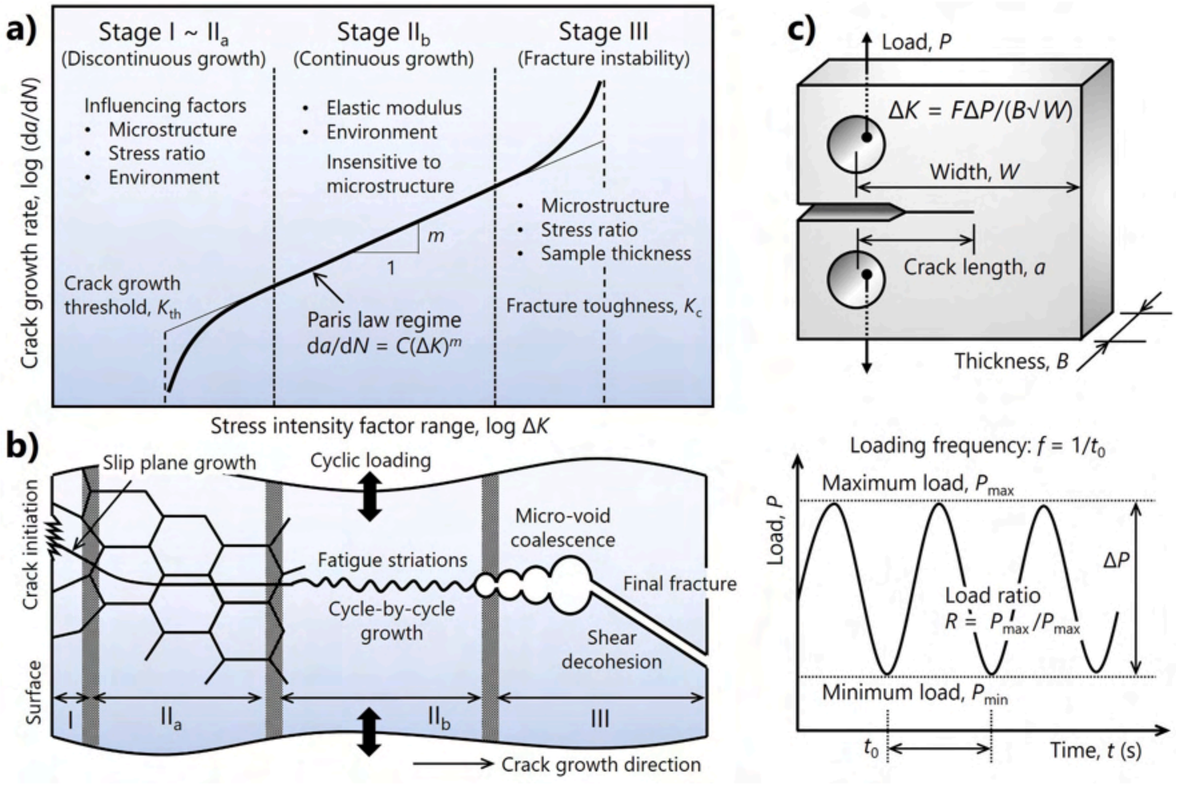

Fig. 1. Schematics of general fatigue fracture processes in structural metals [49,58] and the procedure of FCG test: (a) ΔK-dependent three stages of FCG; (b) microscale failure mode in each FCG stage; and (c) CT specimen configuration and loading form. A significant H-effect manifests in Stage II_b, where logarithmic linearity between stress intensity factor range, ΔK and FCG rate, da/dN, obeys, known as Paris law.

Table 1
List of the primary papers related to HA-FCG in ferritic iron and steels under a gaseous H_2 environment. Information about the examined materials and testing conditions in each paper are included together (NA: no answer, RT: room temperature).

Year	Author	Material	Primary alloying elements	Microstructural character	Yield strength	H_2 gas Pressure	Temp.	Frequency f	Load ratio R
			(mass %)		(MPa)	(MPa)	K	Hz	–
1980	Wachob [66]	SA516	NA	Ferrite-pearlite	330	6.9	RT	1	0.15
1982	Suresh [67]	SA387	2.5Cr–1Mo−0.12C	Ferrite-bainite	290	6.9	296	0.5–50	0.15–0.75
		SA516	1.2Mn-0.23C	Ferrite-pearlite	330				
1985	Cialone [42]	X42	0.8Mn-0.26C	Ferrite-pearlite	~360	6.9	RT	1	0.1–0.8
1991	Cotterill [41]	BS4360	1.6Mn-0.25C	Ferrite-pearlite	NA	atm	298~353	0.1	0.1
1992	Marrow [59]	XM-27	26Cr–1Mo−0.2Ni	Ferrite	300	atm	303~352	0.1	0.5
1997	Fukuyama [68]	S35C	0.7Mn-0.2Si−0.37C	Ferrite-pearlite	310	1.1–9.9	293	0.01–10	0.1
2011	San Marchi [69]	X80	0.4Cr-0.1Nb−0.1Mn-0.2Si-0.05C	Polygonal/acicular ferrite	~590	21	RT	0.1, 1	0.1
2011	Nishikawa [70]	S10C	0.4Mn-0.2Si−0.13C	Ferrite-pearlite	200	0.18	313	0.1, 6	−1
2013	Somerday [44]	X52	0.9Mn-0.1Si−0.06C	Ferrite-pearlite	430	21	295	0.001–10	0.1, 0.5
2014	Drexler [60]	X70	0.2Cr-1.5Mn−0.2Si-0.05C	Polygonal/acicular ferrite	~550	5.5, 34	RT	0.01–1	0.5
2014	Slifka [43]	X52	0.9Mn-0.1Si−0.06C	Ferrite-pearlite	430	7~48	RT	1	0.5
		X100	0.5Ni-1.9Mn−0.1Si-0.06C	Acicular ferrite-bainite	790	1.7–21		0.1, 1	
2016	Ronevich [53]	X65	1.5Mn-0.3Si−0.08C	Banded ferrite-pearlite	480	21	295	1	0.5
2017	Koyama [71]	IF steel	NA	Ferrite	95	0.18	313	0.001–6	−1
2017	Yamabe [45]	SM490B	1.4Mn-0.4Si−0.16C	Ferrite-pearlite	360	0.1–90	RT~423	0.001–10	0.1
2018	Matsuoka [72]								
2018	Wang [73]	SS400	0.5Mn-0.2Si−0.16C	Ferrite-pearlite	310	1, 40	RT	1	0.1
2018	Birenis [74]	Pure Fe	0.07Mn-0.001C	Ferrite	130	0.7, 90	RT	1	0.1
2019	Shinko [75]	Armco Fe	0.14Ni-0.05Mn−0.001C	Ferrite	170	3.5, 35	RT	0.2–20	0.1
2022	Ogawa [55]	S25C	0.5Mn-0.2Si−0.25C	Banded ferrite-pearlite	250	0.7, 90	RT	0.01–1	0.1
		S55C	0.6Mn-0.2Si−0.54C		290				

standardized in the ASTM-E647 [80]. Amongst them, compact-tension (CT) specimens with three characteristic dimensions: width, W; thickness, B; and crack-length, a (Fig. 1 (c)), are most widely employed. The stress intensity factor range is given by the following Eq. (1), where F is the geometry-dependent factor defined as a function of a/W [80].

$$\Delta K = F\frac{P_{\max} - P_{\min}}{B\sqrt{W}} = \frac{F\Delta P}{B\sqrt{W}} \tag{1}$$

In Fig. 1 (a), a typical da/dN-ΔK curve with three characteristic domains in structural steels [49] is schematically shown together with the primary influencing factors in each domain. The corresponding crack propagation modes are presented in Fig. 1 (b) [58]. It is known that the influence of H is relatively small at the regime of slow propagation or threshold (or growth of mechanically/microstructurally small crack), called Stage I ~ II_a [52,67,81]. Available experimental information about this near-thershold regime is very limited due to the long period required for data acquisition. The negative H-impact then starts to appear in Stage II_b, wherein da/dN-ΔK exhibits a power law relationship, well-known as Paris law, *i.e.*, $da/dN = C\Delta K^m$, where C and m are material constants. In fact, dramatic increases in FCG rate, as well as sometimes characteristic crack propagation stages specific to the H_2 gas environment, are evident in most ferritic iron and steels [44,45,59,60,74,67,75].

An example of Stage II_b da/dN-ΔK curves in pure iron [76] and a hot-rolled 0.16% carbon steel with ferrite-pearlite microstructure [45] in air and 0.7 MPa H_2 gas at room temperature are shown in Fig. 2. The FCG rate in air obeys linear logarithmic relationship according to the

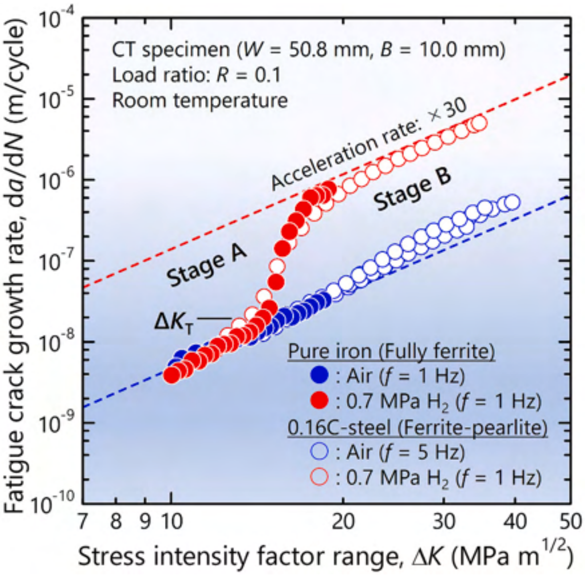

Fig. 2. da/dN-ΔK curves of pure iron [76] and 0.16% carbon steel [45] in air and 0.7 MPa H_2 gas at room temperature (reproduced from Ref. [76]). The graph represents the two-stage H-effects on the FCG rate, which has been found in a majority of ferritic iron and steels.

Paris law. Meanwhile, clear two-stage behavior is identified in H_2 gas: an abrupt increase in FCG rate takes place when the ΔK reaches around 15 MPa $m^{1/2}$. Fig. 3 (a)-(c) show the schematic diagrams for typical H-related or other environmentally assisted cracking behaviors in steels [52,62]. A two-stage crack propagation curve like Fig. 2 can occur (Fig. 3 (c)) when the subcritical crack growth component (Fig. 3 (b)) overwhelms the cyclic crack growth component (Fig. 3 (a)) beyond the static fracture threshold in H_2, K_{IH}. However, it should be emphasized that the sudden increase in FCG rate in Fig. 2 occurs at a stress intensity well below K_{IH} in this kind of low-to-moderate strength materials. Hence, the two-stage HA-FCG in Fig. 2 is fundamentally different from the well-known transitional behavior in Fig. 3 (c). In fact, K_{IH} in ferritic steels with yield stresses less than 500 MPa is greater than 50 MPa $m^{1/2}$ in H_2 gas with pressures below 10 MPa [26,67]. Such a subdivision of HA-FCG stages below K_{IH} was first discovered by Suresh and Ritchie [67], although their study included martensitic and bainitic materials with relatively low yield strength. They designated this transitional point as ΔK_T or K^T_{max} to distinguish it from K_{IH}. In what follows, these mild/negligible and severe FCG acceleration regimes below and above ΔK_T are called Stage A and Stage B (Fig. 2), respectively. The influences of mechanistic and environmental variables on each of these stages will be overviewed. In the authors' previous publications, Stages A and B in Fig. 2 have confusingly been called Stages I and II [74,76,77,79]. We should note here that these terminologies of Stages I and II in references [74,76,77,79] do not correspond to those in Fig. 1. Such a two-stage behavior comprising Stages A and B seems to be universal for a majority of ferrite-based materials. This has been confirmed in other carbon steels [55,68], ferritic stainless steel [59], and pipeline steels [44,53,60].

2.2. *Influences of environmental and mechanistic variables*

2.2.1. *H_2 gas pressure*

The influence of H_2 gas pressure most clearly appears on ΔK_T (*i.e.*, the transition point from Stage A to B). An example of pure iron is shown in Fig. 4 [79]. The effect of H_2 gas pressure is evident when comparing the data obtained at room temperature (Fig. 4 (a)). As the pressure increases from 0.2 to 90 MPa, ΔK_T monotonically decreases. When the pressure rises close to 100 MPa, a major part of da/dN-ΔK curve is eventually dominated by Stage B crack growth. A result for Armco iron also exhibited a similar tendency [75]. If the microstructure becomes more complex, for example, the mixtures of pearlite and other constituents, the transitional point is somewhat unsharpened and tends to be more gradual [43–45,53,60,68]. Nonetheless, the overall shape of da/dN-ΔK curve and its dependency on H_2 gas pressure are invariable even in 0.16%C steel [45], pipeline steels [82], and other medium carbon steels containing a significant fraction of pearlite [53,55].

The H_2 gas pressure also impacts the magnitude of FCG acceleration in Stage A. Although investigations on this mild acceleration regime are quite limited [77,79,75,83,84], the acceleration rate gradually increases up to 10 times relative to the case of nitrogen (N_2) gas in the room temperature data in Fig. 4 (a). Here, in H_2 gas with pressures below 1 MPa, the FCG rate in Stage A was equivalent to or even lower than that in air. This anomaly may be due to a more significant influence of oxygen or water vapor contained in the laboratory atmosphere [85,86] than the acceleration caused by such low pressure of H_2 gas. Indeed, the FCG curve in N_2, where both oxygen and water vapor are absent, is located below the FCG curve in the air. For a proper evaluation of the effect of high-purity H_2 gas, N_2 or other inert environments may be more adequate references.

Meanwhile, the influence of H_2 gas pressure on the FCG acceleration in Stage B is interestingly small, as an example of 0.16% carbon steel [45] is shown in Fig. 5 (a). The acceleration rate slightly increases until the pressure reaches 1 MPa, then becomes plateau at a value around 20–30. Note, however, that the data in Fig. 5 (a) were all measured at a relatively fast loading frequency of $f = 1$ Hz. As shown later, decreasing the loading frequency increases the detrimental H-effect under high H_2 gas pressures around 100 MPa (Section 2.2.3 and Fig. 5 (b)).

2.2.2. *Temperature*

Temperature is seemingly the most critical influencing factor for the H-assisted crack growth in steels and other structural metals [41,59,79,72,87–91]. This is not only for fatigue but also for static loading [87,89]. Although the experimental results are limited to the temperature range above room temperature, it is well recognized that increasing temperature consistently mitigates the crack growth acceleration in H_2 gas. Particularly, the temperature-effect is significant for BCC iron and steels with low-to-moderate strength [41,59,79,72,88].

The experimental results at 298–423 K under different H_2 gas pressures [79] are shown in Fig. 4 (b) (plotted by diamonds, triangles, and rectangles). With the increase in temperature under a given H_2 gas pressure, the FCG acceleration rates in both Stages A and B are reduced. Besides, the transitional point, ΔK_T, shifts to a higher ΔK. Moreover, the FCG acceleration almost completely disappears at a low gas pressure and an elevated temperature (*e.g.*, 0.7 MPa H_2 at 423 K). It was evidenced that the temperature change in the range of 298~423 K barely affects the FCG rate under the absence of H [79,72]. Thus, such a substantial temperature-effect should be a phenomenon specific to the H_2 gas environment. An identical temperature-effect was found at 300–350 K by Marrow et al. for ferritic stainless steel [59], Cotterill and King for

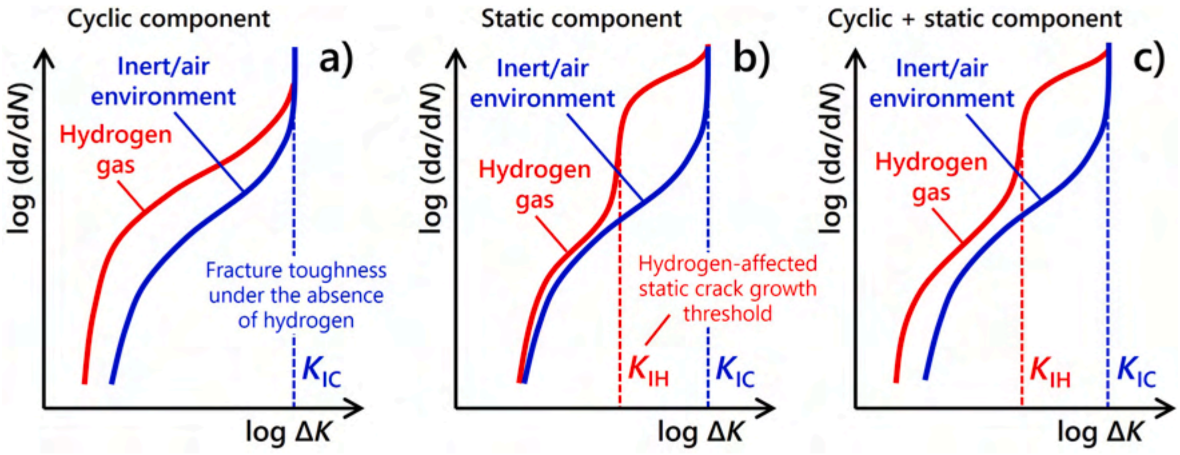

Fig. 3. Schematics of the types of H-assisted fatigue crack propagation behaviors in steels, reproduced from Refs. [52,62]. H may affect either (a) cyclic or (b) static crack growth components depending on the stress intensity level below or above K_{IH}. When both these two occur in a competitive manner, the curve exhibits two-stage behavior like (c).

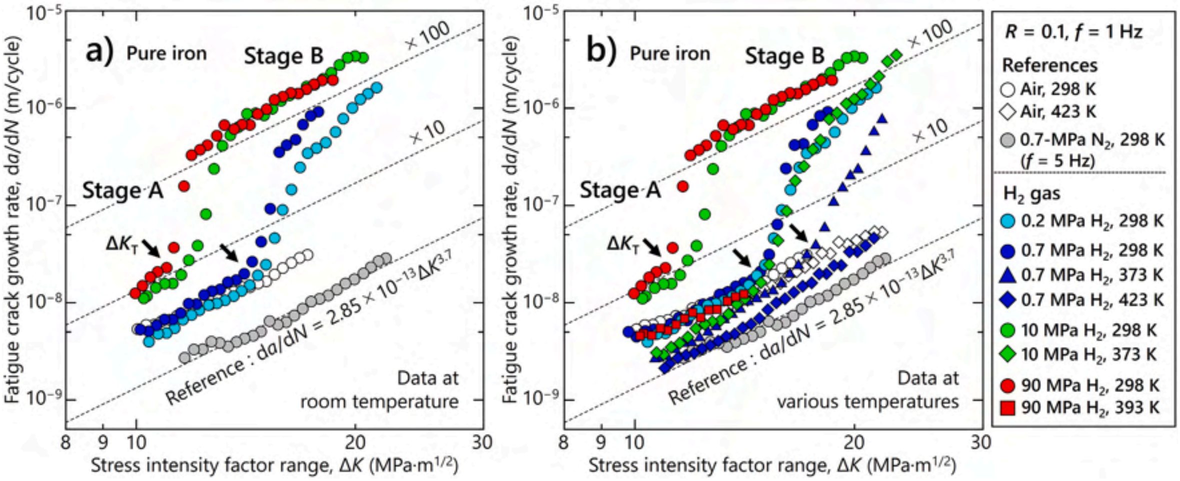

Fig. 4. FCG curves of pure iron in laboratory air, 0.7 MPa N_2 gas, and H_2 gas with various pressures and temperatures (reproduced from Ref. [79]). Only the room temperature data are presented in (a), while (b) includes the results at elevated temperatures.

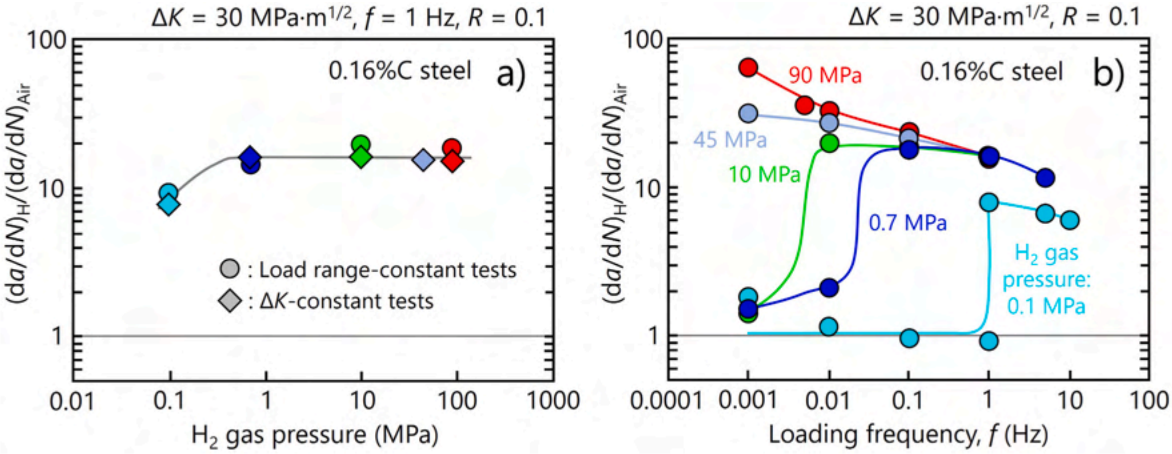

Fig. 5. Relative FCG rate in H_2 gas and laboratory air in a 0.16% carbon steel at Stage B HA-FCG regime ($\Delta K = 30$ MPa m$^{1/2}$, Fig. 2) as a function of (a) H_2 gas pressure and (b) loading frequency (reproduced from Ref. [45]). The data were obtained at room temperature.

4360 ferrite-pearlite steel [41], and Smith and Stewart for 2Ni–Cr–Mo–V rotor steel 88. On the other hand, decreasing the temperature below 300 K also mitigates the crack growth acceleration in a 4130 steel, even though it was only confirmed for static loading conditions [87]. This inverse temperature-dependence below room temperature is possibly due to the delay of H absorption kinetics at the crack-tip.

2.2.3. *Loading frequency*

The load cycling rate in real engineering components is never constant. Thus, from the practical viewpoint, the effects of loading frequency, *f* (Fig. 1 (c)), on the significance of HA-FCG have actively been studied [44,45,56,60,83,88,92–94]. Pressurization and its release are repeated over a time scale of minutes to hours in pressure vessels and pipelines. Accordingly, the HA-FCG behavior at a low loading frequency is of primary importance.

The main target of the studies on such frequency (or loading rate) effects has conventionally been high-strength steels with tensile strengths above 1 GPa [56,62,64,65,94,95]. Such research motivation arises from the strong susceptibility of these materials to delayed fracture in hydrogenating environments [29,32]. H absorption and diffusion kinetics into the crack-tip zone work as a rate-controlling process for the crack growth, giving rise to time-dependent quasi-brittle fracture called subcritical crack growth [29,32]. The crack propagation length is, therefore, a direct function of the loading (or load-holding time) rate and a resultant change in the time for crack-tip opening [62,64,65,95]. This is specifically the case when $K_{\max}$ during the FCG test exceeds K_{IH} (Fig. 3 (b) and (c)), which is very low in high-strength steels (*e.g.*, 20∼ MPa·m$^{1/2}$ [26,29,32]). However, the situation is somewhat different in low-to medium-strength ferritic materials. That is, irrespective of the $K_{\max}$ relative to K_{IH}, subcritical crack growth hardly takes place, and the influence of the loading rate is relatively small [30,96]. The absence of subcritical cracking in low-to-medium strength steels can be proven by the positive slope of their crack growth resistance curve in fracture toughness tests [29,30,35]. A repetition of or further increase in load is a pre-requisite for the growth of the crack: the fracture is macroscopically stable despite an acceleration of the cyclic crack growth component (Fig. 3 (a)).

The acceleration rates in Stage B at $f = 0.001$–10 Hz are depicted for 0.16% carbon steel [45] in Fig. 5 (b). Basically, decreasing *f* leads to a marginal increase in FCG acceleration rate at a relatively high frequency. Then, the acceleration rate eventually tends to saturate at 20–30. No further acceleration occurs as the frequency becomes even lower, a fact also true for all other examined ferritic materials [55,60,70,75,83,93]. Moreover, it is surprising that the FCG acceleration almost entirely diminishes at a low-frequency regime when H_2 gas pressure is lower than 10 MPa. The only exception in Fig. 5 (b) is the behavior in 90 MPa H_2 gas: lowering the frequency to 0.001 Hz still increases the FCG acceleration rate monotonically. Further clarification is required for whether such acceleration eventually saturates, as in the case of lower H_2 gas pressures, or not at an ultra-low frequency regime below 0.001 Hz. Much less attention has been paid to higher frequencies above 1 Hz [44,67,83]. The acceleration would be weakened in such high frequency regime due to the limited time for H absorption into the crack-tip.

For Stage A, where FCG acceleration is relatively mild (Figs. 2 and 4), no detailed investigations into the frequency effects can be found at present. The data for $f = 0.2$–20 Hz range was provided by Shinko et al. for an Armco iron [75]. Their results did not probe any significant dependence of FCG acceleration rate on the loading frequency.

2.2.4. Load ratio

All the author's FCG experiments have been performed with $R = 0.1$ [55,74,77,79]. On the other hand, a higher R such as 0.5 has been employed for the tests of pipeline steels [44,53,60]. This is because the practical pressurization and its release in those components are repeated in the range of 50∼100% of the maximum pressure.

Cialone and Holbrook studied the influence of R on the HA-FCG in X42 pipeline steel, reporting that an increase in R harmfully impacts the FCG rate in H_2 gas at R greater than 0.5 [42]. Such an R-dependence appears because the K_{max} could exceed K_{IH} (Fig. 3 (b)) even under a fixed ΔK when R is sufficiently high. Meanwhile, irrespective of the R value, the dual-stage HA-FCG like Fig. 2 similarly manifests until the K_{max} reaches K_{IH} [42,44,53,67]. It also seems from the literature data that the influence of R on the FCG rate is minor particularly in Stages B unless $K_{max} > K_{IH}$ [42,44,52,67]. When $K_{max} < K_{IH}$, the effect of increasing R only appears as the decrease in ΔK_T [67]. Other possible effects of R are unclear due to the lack of experimental data despite its practical importance.

2.2.5. Impurities in H_2 gas

Aside from the intrinsic H-effects, another factor that affects H-assisted cracking is the amount and species of impurities mixing in H_2 gas. Specifically, large influences of oxygen, methane, acetylene, and carbon monoxide have been documented [30,97,98].

Somerday et al. elaborated on the HA-FCG of an X52 pipeline steel in 21 MPa H_2 gas with various concentrations of oxygen (O_2) [44]. With an addition of only 10 vol ppm O_2, the FCG acceleration is dramatically suppressed. This role of impurities mitigating HA-FCG stems from their premature adsorption onto the crack surface, subsequently inhibiting the adsorption of H [99]. Because the allowable time for impurity adsorption increases with the decrease in loading rate, such an inhibitory effect becomes greater at a low frequency [44]. This has been considered as one of the possible reasons for the disappearance of FCG acceleration in the low-frequency regime (Fig. 5 (b)) when the purity of H_2 gas is insufficient. Even though the impurity effect is outside the main topics of this review, its beneficial effect can positively be utilized for preventing the H-assisted cracking in H_2 gas pipelines and other related facilities by proactive impurity blending.

3. Microscale fracture features

The macroscale phenomenology of HA-FCG in ferritic iron and steels under various mechanical and environmental conditions was overviewed in Section 2. An emphasis was the presence of two crack propagation Stages A and B (Fig. 2). In Section 3, the microscale fracture behaviors in each of these stages are described. They are connected to the deformation microstructures beneath the fracture surface or in the crack-wake.

3.1. Fracture surfaces

Before describing the fracture in H_2 gas, the scanning electron microscopy (SEM) fractographs of pure iron and 0.16% carbon steel after the FCG tests in air are presented in Fig. 6. The fracture surfaces were ductile transgranular (DTG) mode regardless of ΔK, decorated by striation markings perpendicular to the crack growth direction. These features are typical in ductile metallic materials in the Stage II_b FCG domain (Fig. 1) [100–103]. The spacing of the striations is one order of magnitude greater than the macroscopic FCG rate under relatively small ΔK (<20 MPa $m^{1/2}$). Eventually, the striation spacings and FCG rate merge each other after the da/dN increases to 10^{-7}∼10^{-6} m/cycle with an increase in ΔK [100,102]. This correspondence between FCG rate and striation spacing supports the ductile crack growth model involving crack opening and re-sharpening (alternate slip-off model), which will be later shown in Section 4.3.1.

In Fig. 7, the overall appearances of the CT specimens of pure iron tested in room temperature air and H_2 gas are displayed. Relatively dark fracture surfaces are observed in the Stage A region in H_2 gas, as well as in air. However, a fracture surface color in H_2 gas sharply changes from dark to bright at the transition from Stage A to B, implying a prompt change of fractographic characters at this transitional point.

3.1.1. Stage A: Intergranular fracture

What characterizes Stage A in H_2 gas (Fig. 2) is intergranular (IG) fracture [44,77,68,75], which is mixed with ordinary DTG (Fig. 6). Considering the insignificant FCG acceleration in Stage A (Fig. 2), the presence of IG is quite surprising since it is generally understood that IG is one of the brittle and catastrophic failure modes [33,89,104–107]. Fig. 8 shows the SEM images of the Stage A fracture surfaces in pure iron after measuring the data in Fig. 4 (a) [79]. At room temperature, the total fraction of IGs on the fracture surface, $Area_{IG,}$ increases with an

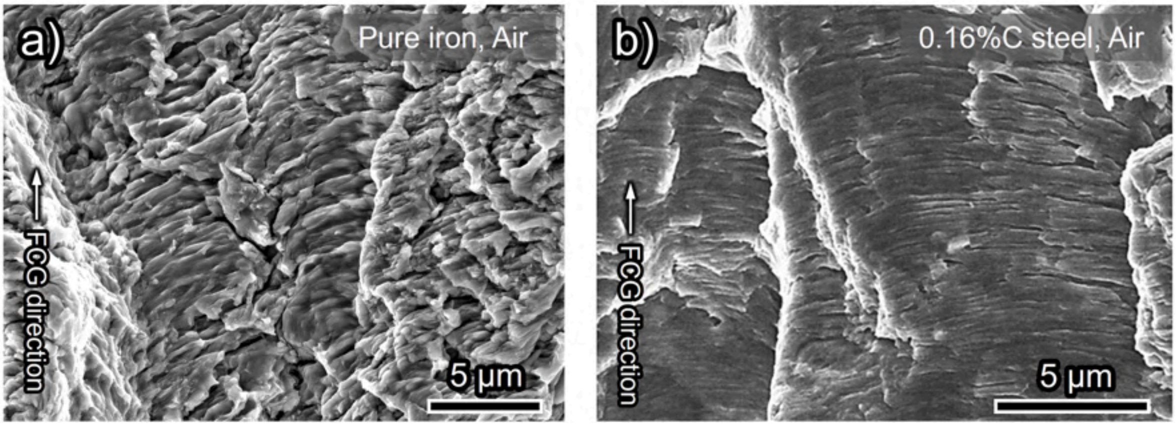

Fig. 6. SEM fractography of (a) high-purity iron and (b) 0.16%C steel tested in laboratory air at the ΔK of (a) 17 MPa $m^{1/2}$ and (b) 30 MPa $m^{1/2}$, showing ductile transgranular (DTG) fracture with striation markings perpendicular to the FCG direction (reproduced from Refs. [45,79]).

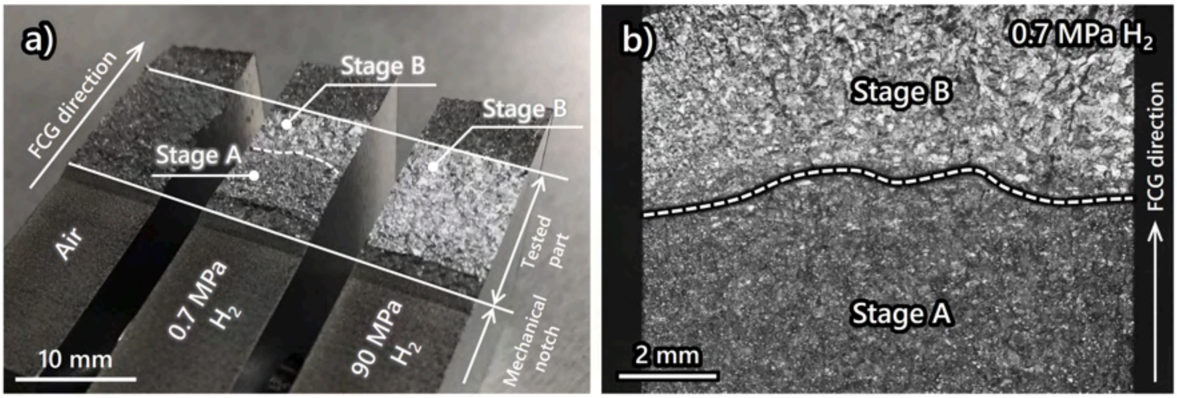

Fig. 7. Macroscopic appearances of the CT specimens of pure iron tested in air, 0.7 MPa H_2, and 90 MPa H_2 at room temperature. (b) magnifies the region corresponding to the Stage-A-to-B transition in the specimen tested in 0.7 MPa H_2 (*i.e.*, the middle one in (a)).

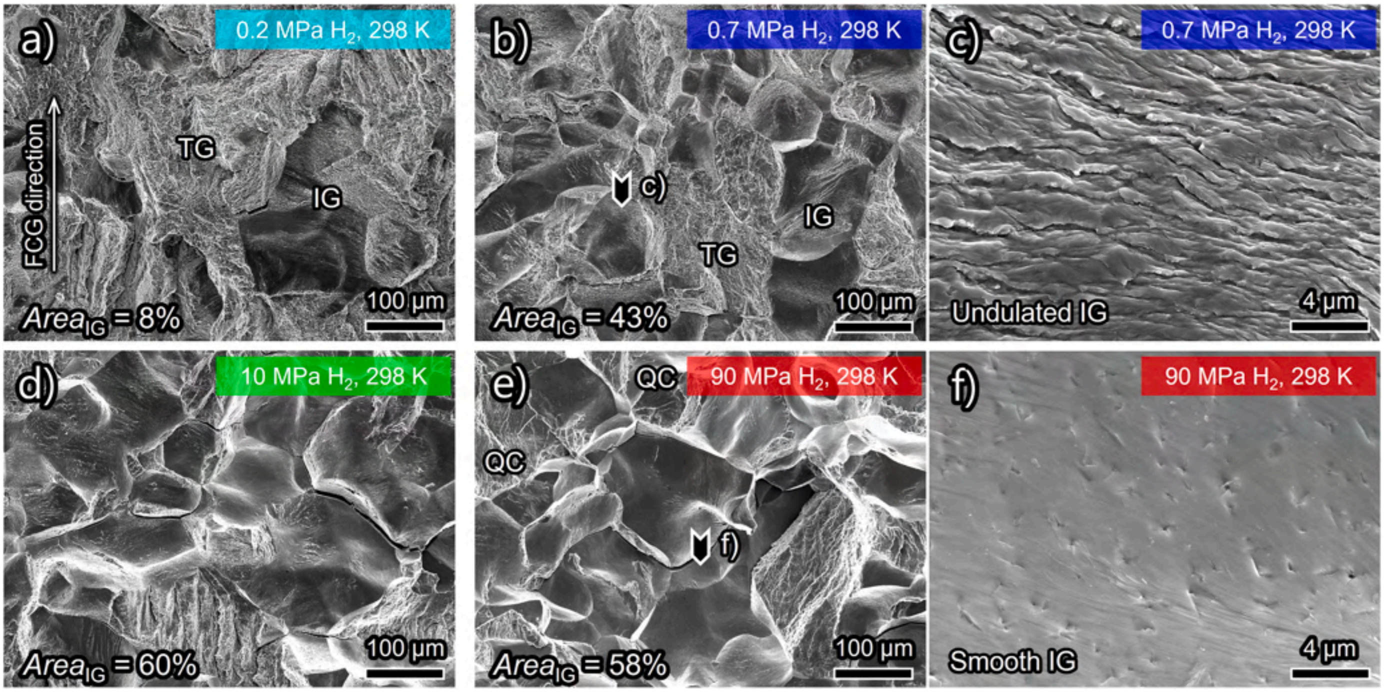

Fig. 8. SEM images of the fracture surfaces in (a) 0.2, (b)(c) 0.7, (d) 10, and (e)(f) 90 MPa H_2 gas at room temperature (298 K), under $\Delta K = 11$ MPa $m^{1/2}$ (Stage A HA-FCG) (reproduced from Ref. [79]). The crack growth direction is from bottom to top in each image. Enlarged views of regions denoted by arrowheads in (b) and (e) are presented in (c) and (f). The area fraction of IGs, $Area_{IG}$, is also provided in (a), (b), (d) and (e).

increase in H_2 gas pressure (Fig. 8 (a)(b)(d)(e)). This increase in $Area_{IG}$ is ascribed to the positive interrelationship between H_2 gas pressure and the FCG acceleration rate in Stage A (Section 2.2.1). In other words, these IGs are the trigger of the mild FCG acceleration in Stage A (Fig. 4 (a)).

At a relatively low H_2 gas pressure (*i.e.*, below 1 MPa) with an almost negligible FCG acceleration in Stage A, the IGs are decorated with tiny and striated undulations in the magnified image in Fig. 8 (c). The alignment of these undulations nearly perpendicular to the crack growth direction infers, at first glance, that they are a kind of fatigue striation. However, their wavelength is more than an order of magnitude larger than the macroscopic FCG rate [79,75,108]. Moreover, the concavity or convexity of fatigue striations should have valley-to-valley or hill-to-hill geometrical correspondence between the mating fracture surfaces in terms of their conventional formation mechanisms [58,102,103]. Nevertheless, a hill-to-valley relationship was conversely reported for the case of undulations on IGs in HA-FCG [108].

With an increase in H_2 gas pressure and the resultant escalation of the FCG acceleration rate, the undulated IGs (Fig. 8 (c)) are replaced by relatively smooth IGs (Fig. 8 (f)). These correlations of the microscale characteristics and area fraction of IGs with FCG acceleration rate are not limited to room temperature but are also valid for higher temperatures. As expected from the temperature-dependence of the FCG acceleration rate in Fig. 4 (b), the increase in temperature under a given H_2 gas pressure diminishes $Area_{IG}$ and tends to restore the undulations on IGs [79]. Note that $Area_{IG}$ similarly decreases with an increase in ΔK, finally reaching zero when the crack growth turns into Stage B [77,68].

3.1.2. Stage B: Transgranular fracture

After the disappearance of IGs, the fracture surface is replaced by a well-known HE-related fracture mode in ferritic steels. That is, there appears the transgranular fracture (Fig. 9), which has conventionally been designated as quasi-cleavage (QC) [109–113]. The QC solely predominates the FCG acceleration in Stage B [44,45,53,59,60,75].

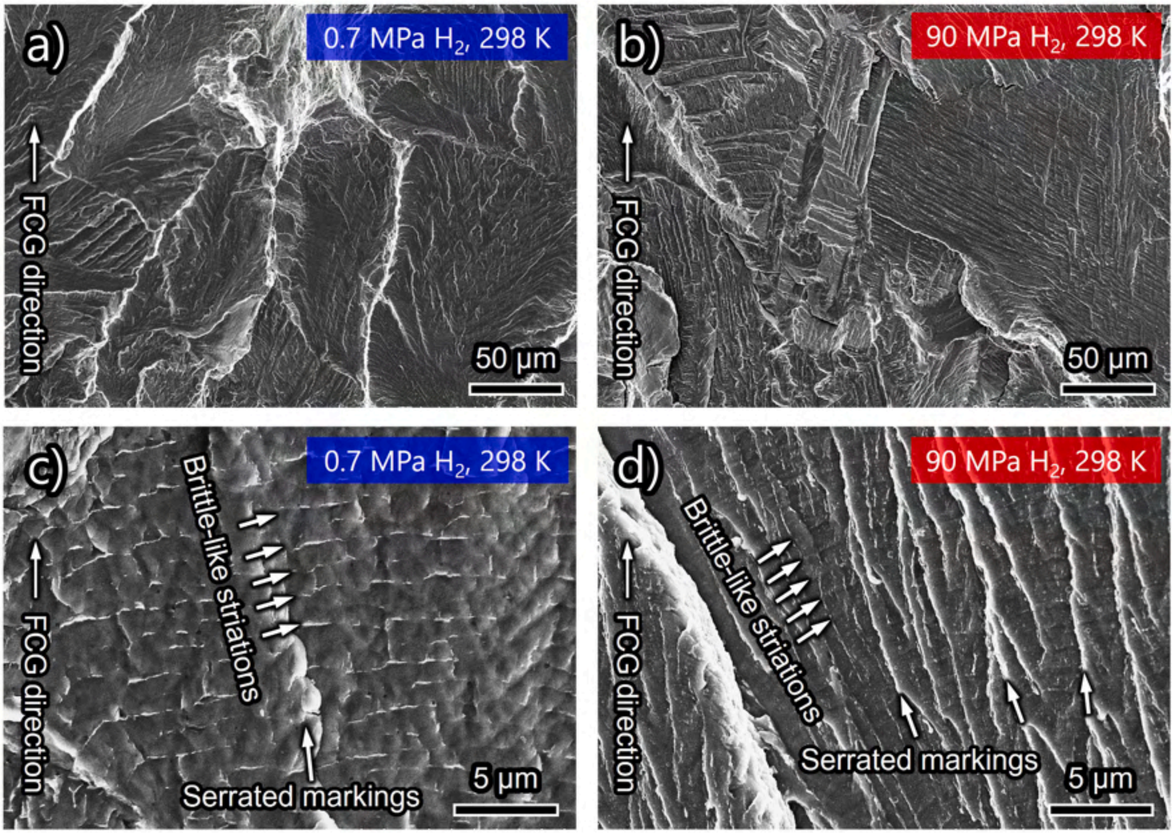

Fig. 9. SEM images of the transgranular fracture surface, which has conventionally been termed quasi-cleavage (QC) in pure iron tested in (a)(c) 0.7 and (b)(d) 90 MPa H_2 gas at room temperature under Stage B HA-FCG regime (reproduced from Ref. [74]). The high magnification images (c)(d) reveal shallow brittle-like striation markings running perpendicular to the FCG direction.

Following this convention, we will also refer to the fracture morphology shown in Fig. 9 as QC for the time being. A more adequate designation alternative to QC will be proposed in Section 3.2.3. In both static and cyclic loading, the surface of QC is usually faceted with the length-scale equivalent to grain size. It is also decorated by river-like ridges (or serrated markings) parallel to the crack growth direction [109,112,114]. The term "quasi-cleavage" originated from its similarity to the ordinary cleavage fracture appearing at cryogenic temperature. However, facet planes of QCs are believed to be not along true crystallographic cleavage planes [109,110,113].

The QCs formed during the HA-FCG in pure iron are displayed in Fig. 9. In addition to the presence of serrated markings, shallow and wide striations perpendicular to the FCG direction (often called brittle- or brittle-like striations [59,75,115,116]) overlapped on the QCs (Fig. 9 (c) and (d)) [45,59,76,74,75,116]. The interspacing of these brittle-like striations coincides with the macroscopic FCG rate [45,74,116], substantiating that each striation line reflects the crack propagation per loading cycle. Despite the weak dependence of the Stage B FCG rate on H_2 gas pressure (Section 2.2.1), higher pressure renders the serrated markings on QCs much more remarkable (Fig. 9 (b) and (d)). All these distinctions seem to be common in both single-phase ferrite and materials having mixed microstructures of ferrite-pearlite [55,74,79]. Moreover, QCs on the fracture surface diminish and are replaced by DTGs (Fig. 6) with the increase in temperature and concomitant decrease in the FCG acceleration rate (Fig. 4 (b)). The disappearance of QCs was confirmed similarly when the FCG acceleration was mitigated at low loading frequencies (Fig. 5 (b)) [45].

3.2. Crack path and deformation microstructures

The microscale process of fatigue crack propagation has been investigated for various metals and alloys *via in-situ* experiments in SEM [117–120]. These efforts were successful in some respects, while technical difficulties against the application of a similar setup to the H_2 gas environment are restricting the progress of our understanding. Despite such limitation, deformation microstructures left behind the crack-tip provide us valuable information to figure out the underlying HA-FCG mechanisms in Stages A and B [74,73,75,121–123]. Here, the microstructural development process without H is first described briefly, followed by how the presence of H changes it.

3.2.1. General process of microstructure development around fatigue crack

The spatial distribution and collective behavior of dislocations in fatigue crack-tip zones have been studied in a wide range of materials employing transmission electron microscopy (TEM) [124–130]. These investigations reported the general trend of dislocations initially being randomly distributed, then transforming into complex arrangements with a decrease in distance from the crack-tip. That is, they transition from discrete loops, tangles, and dipolar bundles into cell structures. In extreme proximity to the crack, more refined dislocation cells or sub-grain structures (*i.e.*, a more evolved state of dislocation cells mutually having well-defined misorientations and sharp boundaries) are generated [129,131]. This development process is reminiscent of low-cycle fatigue of bulk specimens when the strain level shifts from low to high or the number of load cycles increases [132–135]. Namely, dislocation arrangements ahead of the crack-tip qualitatively reflect the distribution of plastic strain and its accumulation level inside the cyclically deformed plastic zone (CPZ).

Based on the formula presented by Birkbeck et al., the size of CPZ, r_c, is expressed as a function of yield stress, σ_y, and K_{max} [136]:

$$r_c = \frac{1}{5.6\pi}\left(\frac{K_{\max}}{2\sigma_y}\right)^2 \tag{2}$$

Substitutions of the yield stresses of pure iron or low carbon steel and the stress intensity range of our present interest ($\sigma_y = 100$–400 MPa and $K_{\max} = 10$–30 MPa m$^{1/2}$) into Eq. (2) yields the r_c of 10^{-5}∼10^{-3} m. Thus, if one considers $da/dN = 10^{-8}$∼10^{-7} m/cycle (Fig. 2), at least hundreds of load cycles are required for the crack to penetrate through the CPZ, which is pre-existing ahead of the current crack-tip location. Note that the CPZ itself also migrates ahead along with the advancement of the crack-tip position. During this process, more dislocations are gradually stored inside the volume located at the leading edge of the initially existing CPZ, as the crack-tip approaches there. The stress level, strain amplitudes, and load cycles applied to the volume also increase simultaneously. Eventually, these stored dislocations exhibit more organized arrangements. When a critical plastic strain is cumulatively reached, they transform into lower-energy configurations (*e.g.*, cells and sub-grains) to minimize their long-range internal stress [137]. A schematic drawing of these development processes is presented in Fig. 10 (a).

Fig. 10 (b)-(e) show an example of dislocation structures around an arrested fatigue crack-tip in pure iron after loading in air, captured by electron channeling contrast imaging (ECCI) in a SEM. In the magnified images, dislocations are sparsely tangled at approximately 40 μm ahead of the crack-tip (Fig. 10 (e)), whereas shortening the distance to 20 μm changes them into cell structures (Fig. 10 (d)). Even though these specific distances should depend on the material's yield stress, the observational facts validate the above description of the development process of dislocations at fatigue crack-tip. In contrast to the dislocation cells formed ahead of the crack (Fig. 10 (d)), a feature behind the crack-tip (crack-wake) was fine sub-grains with relatively large misorientation angles, sharp boundaries, and low interior dislocation densities (Fig. 10 (c)). According to Kuhlmann-Wilsdorf and Hansen, sub-grain structure only forms at the large plastic strain. Increasing misorientation between adjacent dislocation cells cannot sustain uniform plasticity, activating different slip system combinations in each cell [138]. In other words, cell boundaries become sharper, and misorientation angles increase as they operate as not incidental but geometrically necessary boundaries [139]. Awatani et al. found densely tangled dislocations in the region immediately adjacent (∼2 μm) to the fatigue crack-tip in iron. They suggested that those excess dislocations force the uniform cells to transform into finer scale ones or sub-grains 124,140. Such an essential structural change seemingly occurs in the maximum shear stress direction, *i.e.*, ≈70 deg to the crack plane, in addition to the crack-tip environs. This final stage of sub-grain formation is reminiscent of dynamic recovery, as pointed out in Refs. [128,129].

3.2.2. *Deformation microstructures in stage A crack growth*

The IG crack propagation in Stage A is accompanied by substantially evolved deformation microstructures resembling that in the absence of H [77,79,75,121]. Based on the structural development process described in Section 3.2.1, such an evolved state of microstructure is expected since the FCG rate in H_2 gas and that in air/nitrogen are comparable with each other (Fig. 4), especially when H_2 gas pressure is low. At the same time, an evolved microstructure implicates that cyclic deformation and accumulation of lattice defects inside the CPZ play vital roles in the crack to selectively propagate along grain boundaries (GBs).

Fig. 11 (a)-(d) show the cross-sectional EBSD images of the cracks propagated under the ΔK domain corresponding to Stage A in air and H_2 gas with a relatively low pressure of 0.7 MPa at room temperature [77]. The growth rates of these two cracks were mutually identical (Fig. 4 (a)). The plastic strain distribution is visualized here as grain reference orientation deviation (GROD), *i.e.*, the misorientation of each analyzed EBSD pixel from the average crystal orientation of its belonging grain, clarifying no critical H-effects on the evolution level of crack-wake plasticity. Fig. 11 (e) magnifies the crack-tip region in H_2 gas by ECCI (*i.e.*, the area surrounded by a rectangle in Fig. 11 (b)). In response to high GRODs, well-defined sub-grains are identified adjacent to the fractured GB, in addition to the presence of tiny micro-voids along the uncracked GB segment. Thin-foil samples were also separately sampled from some arbitral locations of DTG and IG fracture surfaces in air and 0.7 MPa H_2 by focused-ion beam (FIB) machining. These samples were observed by TEM as shown in Fig. 11(f) and (g) [77]. Sub-grains with sharp boundaries beneath the IG crack are clearer in the TEM image (Fig. 11 (g)). The edge of the crack in TEM sample is wavy, reflecting the

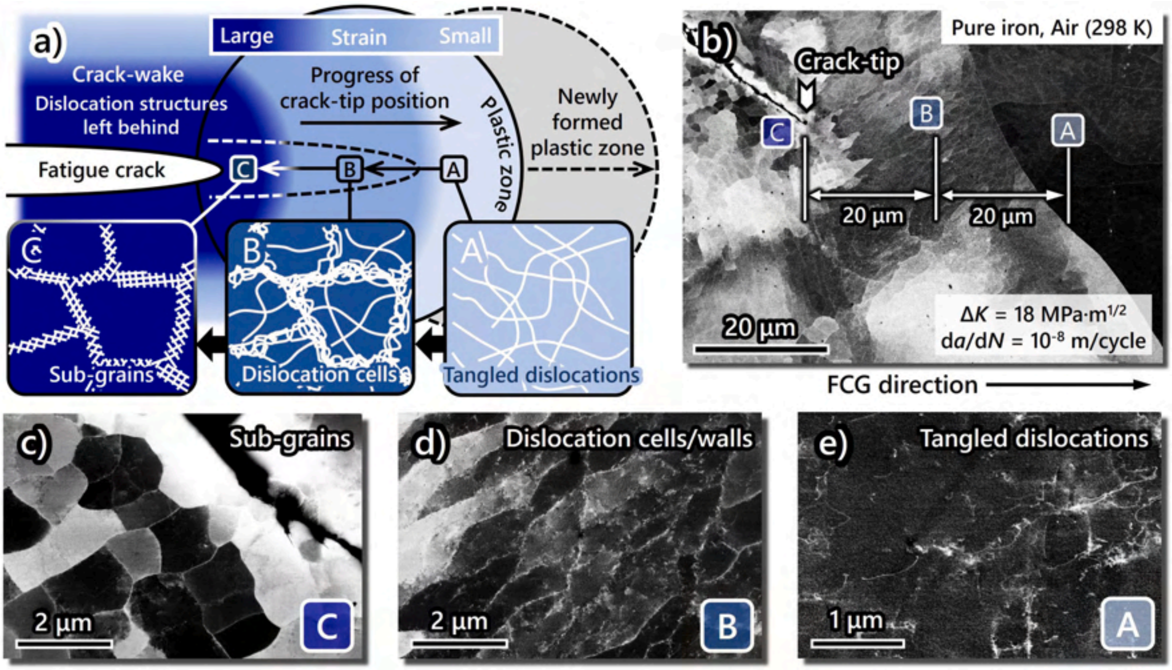

Fig. 10. (a) Schematic illustration of the development process of dislocation structures in CPZ. (b)∼(e) Electron channeling contrast images (ECCI) around the fatigue crack-tip of pure iron terminated in ambient air at $\Delta K = 18$ MPa m$^{1/2}$. (c)∼(e) magnify the three regions marked as A∼C in (b): the positions with different distances from the crack-tip.

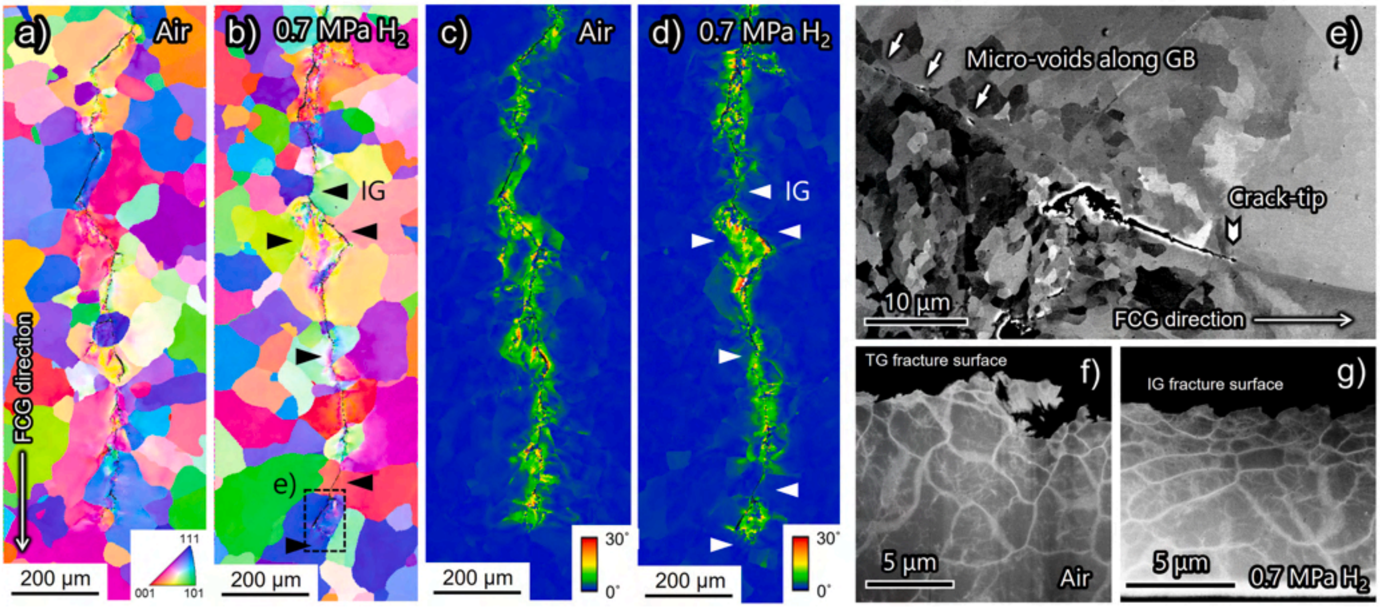

Fig. 11. (a)~(e) cross-sectional images, captured by (a)~(d) EBSD and (e) ECCI, of the fatigue cracks grown in (a)(c) laboratory air and (b)(d)(e) 0.7 MPa H_2 gas at 298 K under $\Delta K = 12$ MPa $m^{1/2}$ (Stage A HA-FCG regime) and $f = 1$ Hz. (a)(b): inverse pole figure (IPF) maps, (c)(d): grain reference orientation deviation (GROD) maps, (e): ECCI of the region surrounded by a rectangle in (b). Arrowheads in (b) and (d) mark the IG fracture paths. (f) and (g) are dark-field scanning TEM images of the dislocation structures beneath (f) DTG fracture surface in air and (g) IG fracture surface in 0.7 MPa H_2 gas at 298 K (reproduced from Ref. [77]).

undulations observed in the fracture surface image (Fig. 8 (c)). With the increase in H_2 gas pressure and a resultant slight increase in the FCG acceleration rate, dislocation structures beneath IG tend to remain somewhat a less evolved state than those shown in Fig. 11 (e) and (g) [77,79].

As expected from the smooth appearance of IG in higher pressure H_2 gas (for example, 90 MPa: Fig. 8 (f)), undulations on the edge of the IG crack are also smoothened, although they still more or less exist (Fig. 12 (a) and (b)). Nonetheless, dislocations are still organized into cells even in such cases (Fig. 12 (a)) [79]. Along the GB located ahead of the IG crack-tip, a nano-scale void is notably observed (Fig. 12 (c)). From the position close to this nano-void and the crack-tip, white contrast (traced

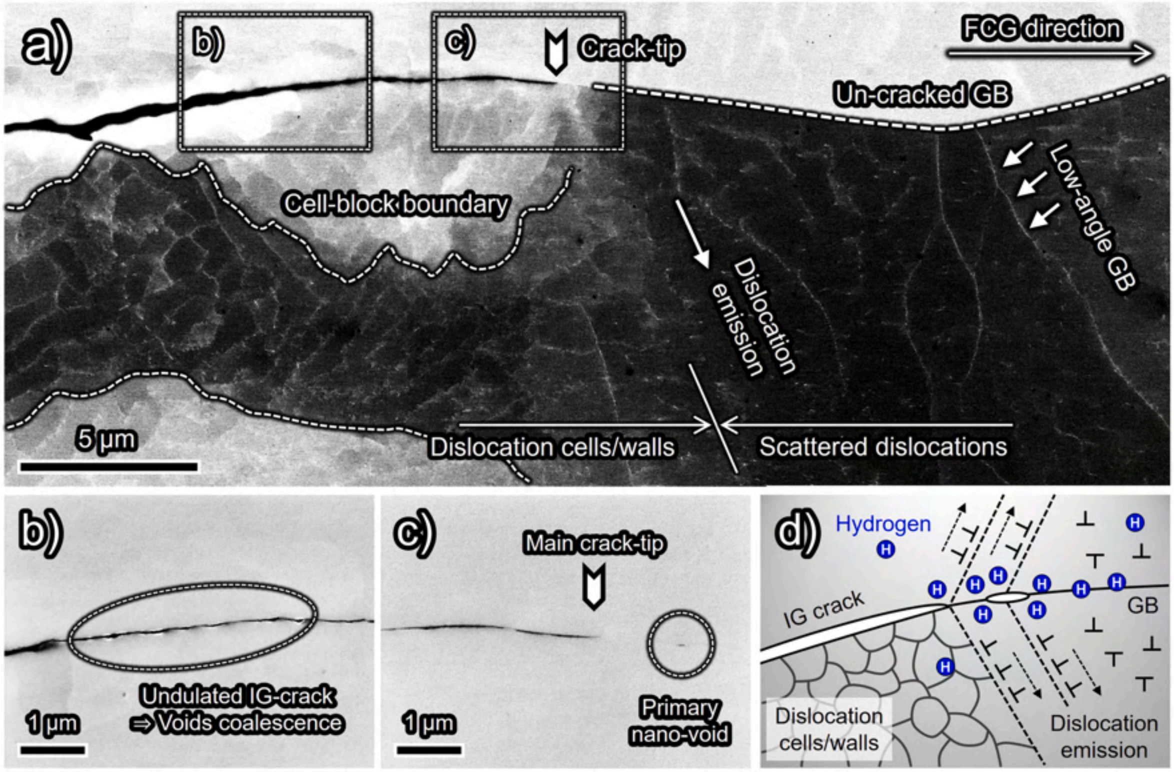

Fig. 12. (a) ECCI and (b)(c) SEM images in the proximity to an IG crack-tip propagating in 90 MPa H_2 gas at 298 K under $\Delta K = 10.5$ MPa $m^{1/2}$ [79]. (b) and (c) are the magnifications of the regions surrounded by rectangles in (a). A correspondent illustration of the IG crack-propagation process is drawn in (d).

by an arrow in the center part of Fig. 12 (a)) aligned almost 70 degrees from the crack plane (*i.e.*, along the maximum shear stress direction) emanates. This white contrast infers the activities of dislocations that are emitted potentially from the crack-tip or near-crack-tip GBs.

3.2.3. *Deformation microstructure and crystallography in stage B crack growth*

The evolution state of dislocation structures beneath the QC in Stage B is largely different from Stage A [76,74]. According to the descriptions in Section 3.2.1, its primary reason is an order of magnitude greater FCG acceleration rate in this second stage of HA-FCG (Figs. 2 and 4). In Fig. 13, the fatigue crack in air and H_2 gas at the Stage B ΔK domain are presented for a 0.16% carbon steel as the optical microscopy images on the lateral surface of a CT specimen [45]. A significant plastic deformation around the crack causes an intricate surface shape in the case of air (Fig. 13 (b)), while the surface around the crack-wake in H_2 gas remains relatively smooth (Fig. 13 (c)).

Such a lesser degree of deformation around the crack in H_2 gas has often been attributed to the latent effect of solute H on the dislocation mobility/character and resultant localization of plasticity into the crack-tip [45,72,92,141–143] (refer to Section 4.3.1). However, one must remember that the plasticity evolution around a fatigue crack is inherently affected by plastic strain cycles applied to the CPZ (Section 3.2.1). If the FCG rate becomes faster under a given ΔK, the crack passes through the CPZ, which extends in front of the present crack-tip position, with fewer loading cycles. This inevitably reduces the plasticity accumulation in the crack-wake region like the appearance in Fig. 13 (c). Thus, the change of the crack-wake morphology in Fig. 13 could be a superficial effect caused by the faster FCG rate itself. It should not be taken as direct evidence supporting the intrinsic H-effects on the crack-tip dislocation activity. At a low loading frequency where the FCG acceleration rate decreases (Fig. 5 (b)), the intricate crack-wake similar to that in air can be observed even in H_2 gas (Fig. 13 (d)) [45].

The morphological difference in the crack-wake plasticity observed by optical microscopy (Fig. 13) is reinforced by EBSD, ECCI, and TEM observations. As some examples are presented in Fig. 14, the crystal misorientation around the crack in H_2 gas is dramatically decreased in the GROD analysis (Fig. 14 (d)-(f)). This is opposed to the case of Stage A crack growth (Fig. 11). The crack in H_2 gas straightly penetrates through each crystalline grain and slightly kinks when it encounters GBs (Fig. 14 (b) and (c)) [76,74].

Fig. 14 (g)-(i) depict TEM images of the thin-foil samples site-specifically extracted from the portions marked A~C in Fig. 14 (a)(b)(d)(e) [76]. It should be noted that the planes of foils in Fig. 14 (g)-(i) are right-angle to the observational planes of EBSD (*i.e.*, foil normal is parallel to the observational plane in Fig. 14 (a)(b)(d)(e)). In the neighbors of straight crack segments with low GROD values (Fig. 14 (i)), only tangled or isolated dislocations are visible without evolved dislocation cells or sub-grain structures. When samples were extracted perpendicularly from the QC fracture surface, slip bands or dislocation walls emanating from the brittle-like striation lines into the maximum shear stress direction were sometimes confirmed in other studies [121,123]. Those slip bands are accompanied by diffusely developed dislocation cells as a background (Fig. 15) [74,121,123].

Another notable feature of Stage B HA-FCG is its crack path crystallography. Although the analysis was performed only two-dimensionally, considerable parts of the crack path in H_2 gas are along {001} cleavage plane of BCC, as determined by the plane traces superposed in Fig. 14 (a)-(f) [74]. Such a cleavage fracture is three-dimensionally supported by TEM if one compares electron diffraction patterns in Fig. 14 (i) with the edge of the thin-foil sample that corresponds to the fracture surface. There has been a common understanding that the H-induced QCs in BCC iron and steels are different in their nature from the conventional cleavage appearing at cryogenic temperatures 109,110,112,113. However, the cracking mode during Stage B HA-FCG, which has also been designated as QC [42,73,116], more or less contains the fracture along the real crystallographic cleavage plane. On the basis of this essential discovery, the term QC is hereafter redefined as "*cleavage-involving transgranular (CIT)*" fracture in the present paper. Notably, the emergence of such true cleavage coincides with the past static loading experiments reporting the H-induced {001} plane fractures in single crystals of pure iron and Fe–Si alloy when those specific planes were nearly perpendicular to the loading axis [144–147]. As the H_2 gas pressure becomes higher close to 100 MPa, the HA-FCG along {011} plane tends to be intermixed with {001} [55]. Similarly, other studies also clarified the persistent H-assisted fractures along some specific crystallographic planes of BCC [113,148–151], although its reason is unclear at present.

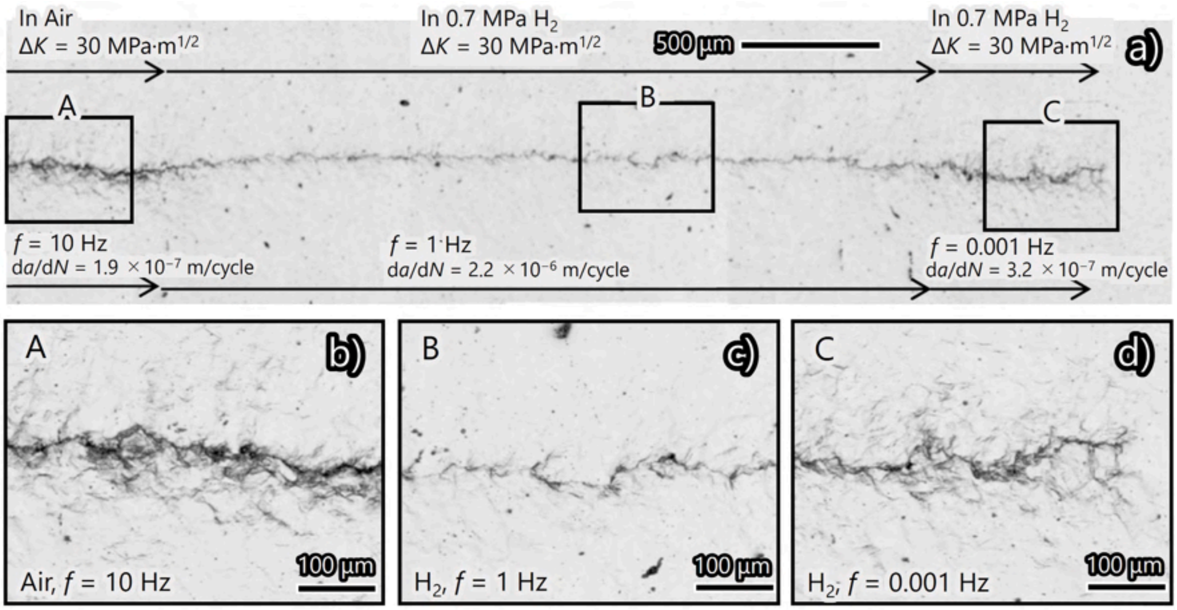

Fig. 13. Optical microscopy images of the crack-wake of 0.16% carbon steel on the specimen surface after environment-switching FCG tests between laboratory air and 0.7 MPa H_2 gas at 298 K (reproduced from Ref. [45]). (a) is an overall image, while (b)~(d) magnify the regions A~C in (a). The crack propagated from left to right.

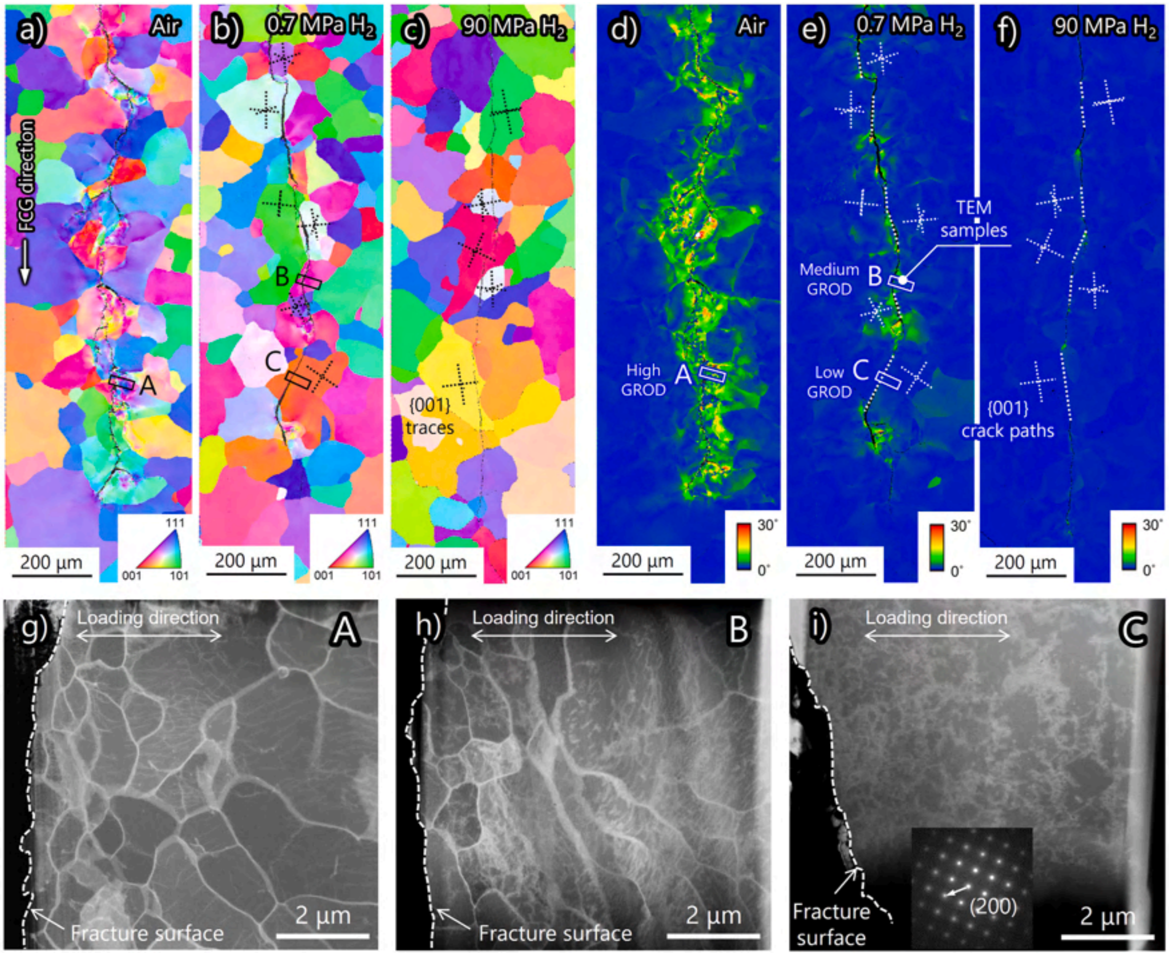

Fig. 14. (a)~(f) cross sections of the fatigue crack paths in pure iron tested in (a)(d) air, as well as in (b)(e) 0.7 and (c)(f) 90 MPa H_2 gas at 298 K under $\Delta K = 17$ MPa $m^{1/2}$ (Stage B HA-FCG) (reproduced from Refs. [76,74]): (a)~(c) IPF maps; (d)~(f) GROD maps. Thin-foil samples were extracted from the positions marked A~C in (a)(b)(d)(e), and their dislocation structures were observed by scanning TEM as shown in (g)~(i).

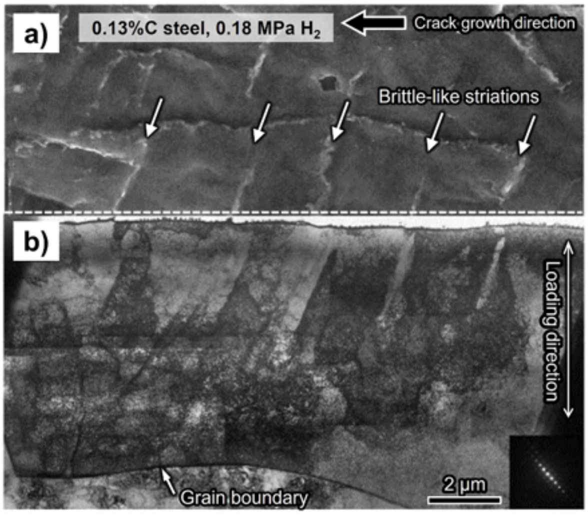

Fig. 15. Micrographs of a QC (or CIT) facet in a 0.13% carbon steel (reproduced from Ref. [123]): (a) SEM image showing brittle-like striations (indicated by arrows); (b) cross-sectional TEM image beneath the fracture surface at the position of the dotted line in (a). An electron diffraction pattern is contained in the inset of (b).

4. Controlling mechanisms

4.1. Fundamentals of H-material interactions

The phenomenological survey in Sections 2~3 highlighted the dual-stage HA-FCG in ferritic iron and steels: Stages A and B. Each stage exhibited characteristic fracture modes and crystallographic fracture pathways, giving rise to an order of magnitude difference in FCG acceleration rate and its dependencies on a variety of mechanistic and environmental variables. These overall tendencies are not specific to pure iron, but rather general in multiple material systems 44,45,55,59,60. Such universality of HA-FCG behavior demonstrates that the underlying failure mechanisms are identical as long as the principal microstructural constituent is ferrite.

Toward the understanding of HA-FCG mechanisms in Stages A and B, one should first recall potential changes in basic material properties when H is involved. Since the 1970s, a number of papers have addressed the essential H-impacts in iron and steel, establishing three prevailing aspects.

(i) H-enhanced decohesion [152–156]: atomistic cohesive energy along a cleavage plane, GB, or interphase boundaries is weakened by H.

(ii) H-effects on plasticity [73,142,157,158]: H atmosphere around dislocations affects the mobility, character, and collective behavior of those dislocations.

(iii) Point defect multiplication [159–162]: atomic vacancies, free volumes, and their clusters are energetically stabilized by H.

Depending on the material's strength and loading condition, either of (i)~(iii) becomes predominant. Or in most situations, several of them synergistically operate and complexly interact with each other [142, 163,164]. Detailed descriptions of these fundamental models can be found in other reviews 142,158,159,164. Fig. 16 illustrates some H-induced deformation and fracture events potentially emerging inside a crack-tip zone due to the above models (i)~(iii). In what follows, plausible failure mechanisms, that can consistently rationalize the HA-FCG characteristics described in Sections 2~3, are discussed with the aid of supplemental validations.

4.2. Intergranular crack growth: Stage A

4.2.1. Grain boundary-damaging model

To the authors' knowledge, the process of IG HA-FCG in ferritic steel was first elaborated by Nishikawa et al. [108], although the result was not correlated with fracture mechanics parameters (*e.g.*, *K*) due to the special specimen configuration they used. Their most notable finding was that the IG fracture commences after a damage nucleation along the GB located close to the crack-tip, where dislocation slip bands emanating from the intragranular region are impinged. The finding agrees well with the authors' observation result of micro-voids along GBs in Figs. 11 and 12. Later, Koyama et al. reached a similar conclusion for interstitial-free steel and ascribed those GB damages to the fine undulations found on the IG fracture surface (Figs. 8 (c) and Fig. 11 (g)) [71]. Based on the striated morphology of these IG undulations, they deduced that GB micro-voids in the two-dimensional image have three-dimensionally tunnel-like shapes. Such a tunnel-like form of IG micro-voids is plausible if one considers that the damages can be nucleated along the intersections between GBs and planar slip bands [108].

In general, GBs maintain their sufficient integrity even after significant plasticity. Meanwhile, they work as both absorption and nucleation sites for dislocations [165,166], as well as serving as trap sites for H atoms [12,23,167,168]. Additionally, the coordinative motion of dislocations with their H atmosphere [169,170] may transport intragranular solute H to GBs. This can be an extra factor in triggering the temporal accumulation of H during the deformation [142,171]. Recent molecular dynamics (MD) simulations demonstrated the nucleation of atomic-scale free volumes along GBs in Fe and Ni when such incorporation/emission of dislocations occurs along H-segregated GBs [172–174]. They adopted the results into the H-assisted point-defect accumulation model [159,175]. These free volumes eventually grow into micro-voids as the GB-dislocation interactions are repeated within the slip bands. The coalescence of those grown-up micro-voids finally encompasses the boundary decohesion. Notably, this type of GB fracture progresses more readily with an increasing amount of segregated H 172, 173.

Within the volume in front of the fatigue crack in H_2 gas, GB damage nucleation and accumulation *via* severe cyclic straining is conceivable in the course of the microstructural development process described in Section 3.2.1. When the crack-tip approaches close to those pre-damaged GBs, they become the weakest and the most selective propagation pathway for the crack. Moreover, if a GB is located immediately ahead of the crack-tip, the emission of dislocations from this crack-vicinity GB is feasible as simulated by MD [176]. Supposedly, the micro-void ahead of the IG crack-tip and corresponding trace of dislocation activity in Fig. 12 (a) is a consequence of such dislocation emission and resultant damage nucleation, as a schematic drawing is shown in Fig. 12 (d). Once the size and density of these GB damages become critical, IG fracture commences due to the fracturing of the internal ligament between individual damages. The cohesive energy of such internal ligament may also increasingly be weakened by an increasing amount of segregated H [153,154]. Note that similar undulated IG fracture has been observed even in the environment without H at very low ΔK, where CPZ size is equivalent to the grain size [136,177,178]. Under the presence of H, the emergence of IG is somewhat extended to a greater ΔK range due to an enhanced GB damaging effect.

4.2.2. Conformity to the phenomenological findings

According to the above fracture model based on the damaging and cohesive energy reduction along GBs, the tendency of IG fracture and resultant FCG acceleration should be a function of the amount of H segregating into GBs. It is challenging to quantify the amount of local H concentration along the GBs inside the dynamically loaded fatigue crack-tip zone. Nevertheless, a qualitative estimation can be made, if one assumes that the partitioning of H into trap sites obeys the Fermi-Dirac statistics [179].

$$\frac{\theta_x}{1-\theta_x} = \theta_\mathrm{L} \exp\left(\frac{E_\mathrm{B}}{R_\mathrm{U} T}\right) \tag{3}$$

Here, θ_L is the occupancy of interstitial lattice sites by H atoms (*i.e.*, tetrahedral (T-) sites for BCC iron). θ_x is the H occupancy of the trap site, called H-coverage in the case of H-trapping along GBs. E_B is the binding energy of H atoms with the trap site, R_U is the universal gas constant, and T is temperature. The solubility of H in iron was experimentally measured by Quick and Johnson [180], giving rise to the solute H concentration as $C_0 = 0.00185 f_\mathrm{g}^{1/2} \exp(-3440/T)$ in atom fraction. f_g is

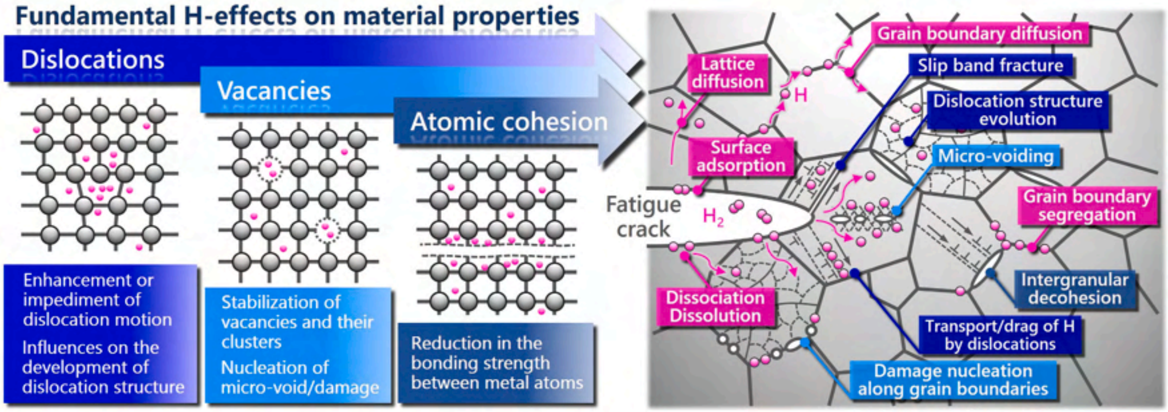

Fig. 16. Schematic illustrations of the fundamental H-material interactions, which have been proposed and well-accepted during these few decades. The right-hand side of the figure denotes some potential phenomena, which can be triggers of H-assisted crack growth, manifesting at the crack-tip zone loaded in a gaseous H_2 environment.

the fugacity of H_2 gas with a unit of atm, which is a function of gas pressure and temperature [39]. Considering six T-sites per Fe atom, it becomes $\theta_L = 9.8 \times 10^{-5} f_g^{1/2} \exp(-3440/T)$ with f_g in MPa. In Fig. 17, the relative FCG rate in H_2 gas in Stage A with respect to that in N_2 gas is plotted versus θ_x. Here, E_B is parametrically varied within 40~60 kJ/mol. Admirably, all the data points under a variety of pressure-temperature combinations are unified into one master curve, when E_B is close to 50 kJ/mol. This value of 50 kJ/mol is, as expected, consistent with the H-GB binding energy in iron determined by experiments and computational analyses [12,167,181,182]. In this context, the physical meaning of temperature-increase to mitigate IG fracture and FCG acceleration (Figs. 4 and 8) is now straightforward. That is, thermally activated desorption of H from the GB trapping sites makes the H-coverage smaller, rendering the GBs less sensitive to damage nucleation and decohesion.

Another noteworthy point in Fig. 17 is that the $(da/dN)_H/(da/dN)_N$-θ_x relationship can be divided into three regimes: (i) $\theta_x < 0.2$ with the absence of FCG acceleration; (ii) $0.2 < \theta_x < 0.6$ where FCG rate gradually increases with θ_x; and (iii) $\theta_x > 0.6$ with a prompt escalation of the FCG acceleration rate. Alongside this tendency, the morphologies of fracture surfaces in H_2 gas transition as follows [79]: (i) absence of IGs; (ii) relatively mild fraction of IGs having undulations on their surfaces (Fig. 8 (a)-(c)); (iii) large fraction of IGs with smooth surfaces (Fig. 8 (d)-(f)). Based on the fracture model in Section 4.2.1, the presence of these three regimes is plausible since the critical strain for the combined establishment of sufficient GB damage size/density and fracture of internal ligament should depend on the GB H-coverage. Namely, a large amount of cyclic deformation may be required for GB damage nucleation, growth, and coalescence (or these events are infeasible) under low θ_x. As a result, just a slight or negligible FCG acceleration and substantial traces of tunnel-like micro-voids on the IG fracture surfaces manifest. Meanwhile, void traces are shallow, and the FCG acceleration becomes much greater under higher θ_x due to the easiness of all the above fracture processes even with a lesser cyclic strain [79].

The GBs, which are involved in CPZ but still certainly distant from the crack-tip, can also preliminary be damaged according to the model in Section 4.2.1. If this is so, the fracture sensitivity of those GBs should permanently be increased even after the sample is extracted after a test interruption in H_2 gas. Such a prognosis has experimentally been demonstrated by Nishikawa et al. [108]. The IG crack propagation indeed continues over a certain distance after switching the test environment from H_2 to N_2.

4.3. *Transgranular crack growth: Stage B*

4.3.1. *Previous models*

Aside from the lack of literature concerning the HA-FCG in Stage A, phenomenological models have been proposed for the transgranular (*i.e.*, QC or CIT) crack growth in Stage B [45,59,74,75,116,183] (Fig. 18). Regarding this latter stage, a much more substantial H-effect on the FCG rate and its practical importance aggressively enhanced the researchers' interests.

The first attempt was made by Marrow et al. on ferritic stainless steel [59] in terms primarily of the H-enhanced decohesion concept [152]. They explained that a local zone with high dislocation density is formed at the crack front. These dislocations significantly trap H and thereby giving rise to micro-scale cleavage in a brittle manner (Fig. 18 (b)). According to this hypothesis, a line of brittle-like striation on the fracture surface (Fig. 9 (c) and (d)) could be the evidence of temporal crack arrest when the cleavage is terminated after the passage of the crack through the locally brittle crack-tip zone. Otherwise, it is formed by a small crack-tip opening at the beginning of the next loading cycle.

Against Marrow's model [59], the research group directed by Murakami and Matsuoka developed a fully plasticity-mediated crack propagation mechanism [185,183] (Fig. 18 (c)). They modified the FCG model developed by Laird and Smith [184], as well as by Bichler and Pippan [103], which originally aimed to explain the formation of fatigue striations in an inert environment in terms of crack-tip opening and re-sharpening: alternating slip-off model (Fig. 18 (a)). The main assumption of Murakami and Matsuoka's model lies in the enhancement of dislocation mobility by solute H in iron, a claim supported by *in-situ* deformation experiments in an environmental TEM [142,157,158]. In the region ahead of the fatigue crack-tip, the presence of dislocations, high hydrostatic stress (*i.e.*, stress-assisted diffusion) [186–188], and continuous supply from the crack surface all contribute to facilitating the condensation of H under a loading phase. Since the dislocation motion is enhanced and the plastic deformation is accordingly localized within this H-accumulated zone, the crack-tip successively advances without significant blunting. Each striation marking on the fracture surface (Fig. 9 (c) and (d)) is formed by a subsequent reverse slip and crack re-sharpening in an un-loading phase. The height of striation becomes shallow due to a lesser degree of crack-tip opening as compared with that in non-hydrogenating conditions. In short, their model is an application of the H-enhanced localized plasticity (HELP) [141–143], which has been proposed as one of the predominant HE mechanisms. They emphasized the optical microscopy images like Fig. 13 as evidence to substantiate their model of H-assisted plasticity localization.

A different plasticity-mediated model was later developed by Nishikawa et al. (Fig. 18 (d)) [116]. The distinction of their model from

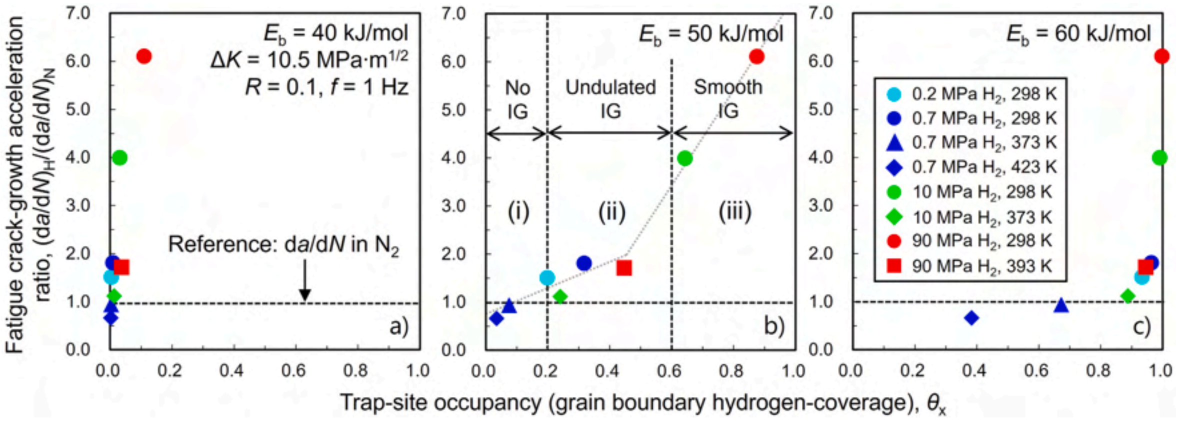

Fig. 17. FCG acceleration rate in pure iron under H_2 gas at various pressures and temperatures with respect to the room-temperature N_2 gas, $(da/dN)_H/(da/dN)_N$, as a function of GB trap-site occupancy, θ_x, determined at a different binding energy with hydrogen, E_B (reproduced from [79]). A good correlation between $(da/dN)_H/(da/dN)_N$ and θ_x was obtained at $E_B \approx 50$ kJ/mol, where $(da/dN)_H/(da/dN)_N$ monotonically increases with an increase in θ_x.

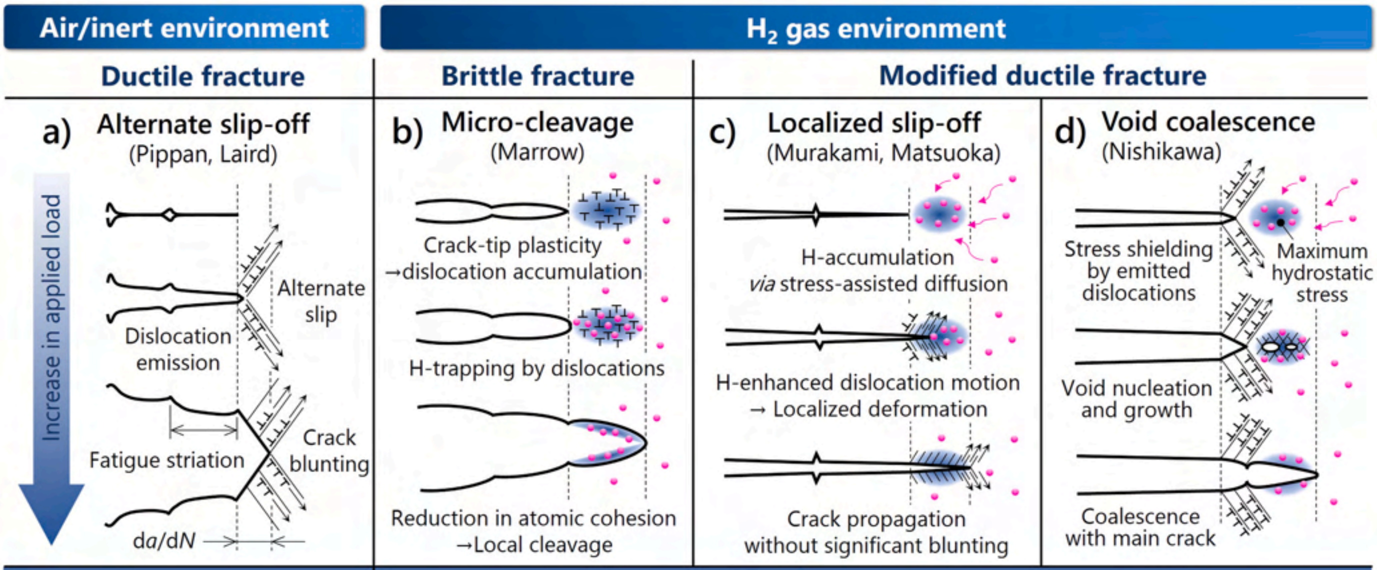

Key phenomenology	Compatibility		
Reduction in the crack-wake plasticity evolution	Compatible	Compatible	Compatible
Selective crack growth along cleavage plane	Compatible	**Incompatible** Localized plasticity alone unlikely to cause {001} type fracture	**Incompatible** No plausible reason for selective void formation along {001} plane
Transitional FCG behavior from Stage A to B	Compatible	**Incompatible** Why is QC surpassed by IG at low ΔK domain?	Uncertain
Mitigation of HA-FCG at low loading frequency	**Incompatible** No reason for the cessation of cleavage	Uncertain	Uncertain
Pressure- and temperature-dependencies of FCG rate	**Incompatible** Cleavage should be enhanced under higher H_2 gas pressure	Uncertain	Uncertain

Fig. 18. Previously proposed models for the transgranular FCG processes involving (a) ductile striations in air or inert environment [103,184], as well as for (b)~(d) transgranular HA-FCG in Stage B with brittle-like striations [59,116,183,185]. The compatibilities of each model to some key phenomenological findings described in Sections 2 and 3 are assessed in the lower table.

others is that they presume micro-void nucleation ahead of the main crack-tip prior to the crack propagation. At the start of the loading phase, the material shows alternate slip (*i.e.*, dislocations emission from the crack-tip) and crack-tip opening. Such alternate slip becomes a localized event under the presence of H like the assumption by Murakami and Matsuoka [185,183,189]. A line of brittle-like striation is formed in this crack-opening process. The long-range internal stress of these emitted dislocations shields the mode I stress-field at the crack-tip [190]. Instead, the location with maximum stress moves to the region slightly ahead of the crack. Once H accumulates into this maximum stress region and locally enhances dislocation mobility [157,158], extensive plastic deformation occurs. Then, micro-voids are nucleated *via* interactions of these dislocations with other slip systems or inclusion particles. The crack propagation takes place by void growth and its coalescence with the main crack. Ultimately, the basis of their model is also on the H-assisted dislocations activity and strain localization within the crack-tip (*i.e.*, HELP [141–143]). What should be appreciated in their study is the extensive efforts to substantiate their own model through various dedicated experiments involving intermittent changes of loading form and test environments.

4.3.2. *Compatibility of the previous models to experimental findings*

For a comprehensive understanding of Stage B HA-FCG, the candidate model can consistently explain all the experimentally identified crack morphologies, fracture surface features, and the dependencies of FCG acceleration on various mechanistic and environmental factors. Specifically, the key points are:

(i) Lesser development of dislocation structure in the crack-wake.
(ii) Crack propagation partially along {001} cleavage plane.
(iii) Presence of the transition from Stage A to B.
(iv) Prompt decrease in FCG acceleration rate at low test frequency.
(v) H_2 gas pressure- and temperature-dependencies of FCG rate.

In Fig. 18, compatibilities of the three previous crack propagation models [59,116,185] to these points (i)~(v) are assessed. All models suit the weakening of dislocation structure development since a faster FCG rate under a given ΔK inevitably leads to the reduction of cumulative plastic strain inside the CPZ (cf. Section 3.2.1). Considering the significance of H-dislocation interactions for both micro cleavage (Fig. 18 (b)) and plasticity localization (Fig. 18 (c) and (d)) models, the mitigation of HA-FCG by an increasing temperature seems to be a natural consequence of thermally activated evaporation of H from dislocations trapping [191]. However, each model includes one or more incompatible points, although they partially conform to some of the above (i)~(v).

Since the H-enhanced decohesion is a positive function of H concentration [153–155,192], Marrow's model [59] predicts a greater magnitude of FCG acceleration in Stage B with an increase in H_2 gas pressure. However, the FCG rate after the Stage A-to-B transition exhibits, in practice, minor gas pressure-dependence (Fig. 5 (a)). Regarding the other two plasticity-mediated models, one cannot find any plausible reasons for the crack selecting specific crystallographic planes such as {001}. Moreover, in the model by Murakami and Matsuoka [45,185,183,189] assuming the change of crack-tip plasticity expansion, the dislocation activity is locally still substantial, which would lead to high misorientation development in the close proximity to the crack. This was not evidenced in our observation in Fig. 14 (*i.e.*, plasticity was merely reduced rather than localized), as well as in the investigation by Wan et al. on Fe–3%Si steel [193]. Besides, considering the plasticity localization only, a dramatic and prompt transition of the fracture mode from IG to CIT is hard to rationalize (Why the fracture mode observed in Stage B does not manifest at low ΔK?). Some recent experiments also criticized the H-induced plasticity localization [194,195]. These studies demonstrated that the overall size of the crack-tip plastic zone is not changed by H, whereas H may affect the plasticity in the limited region close to the crack.

The abnormally mitigated FCG acceleration at a low loading frequency was discussed by Matsuoka et al. [45] and Nishikawa et al. [116] from the viewpoint of H distribution around the crack-tip. In short, they assumed a broadening of H distribution with a slowdown of loading rate (*i.e.*, allowable time for H diffusion). The broader H distribution may relax the severity of H-induced plasticity localization. Note, however, that the H diffusivity in ferrite at ambient temperature is fast (*i.e.*, $10^{-10}\sim10^{-8}$ m^2/s [196,197]) so that the migration of H through the lattice takes place by a distance $10^{-5}\sim10^{-4}$ m or greater within just 1 s. In contrast, the FCG rate in H_2 gas is no more than an order of 10^{-6} m/cycle (Fig. 2). Thus, the H distribution around the crack-tip should already be broad enough even at 1 Hz, when the FCG test is running in a steady-state.

4.3.3. Development of a dislocation-obstruction model

Enhanced dislocation mobility by H, which has been visualized in an environmental TEM [157,158], is still attracting the researchers' attention for explaining many aspects of the H-effects on material properties. Nevertheless, recent developments in computational calculations enabled us to obtain a more straightforward picture of H-dislocation interactions [191,198–203]. These new insights are stirring up a debate over the well-established hypothesis on the role of H in changing the dislocation mobility.

The starting point of computational studies on BCC iron was to calculate an interaction between only one solute H atom and a dislocation line [204,205]. It was in the 2010s that the calculation became feasible for synergistic interactions with multiple H atoms under a more realistic H concentration and time scale [191,198,200,206]. The first pioneering study was performed by Song and Curtin [198]. They demonstrated that the dragging force by the H atmosphere slows down the movement of an edge dislocation under a given applied stress. Similar verifications have later been carried out [200–203,206], reaching an identical conclusion that H can obstruct dislocation motion rather than enhance it. Only in some very limited cases (*e.g.*, when H concentration and applied stress were both extremely low; or when the deformation is controlled by kink-pair formation rate on a screw dislocation line), an enhancement of dislocation mobility by H can be observed [191,199,201,207,208]. In relation to the present review, one has to emphasize the most recent paper by Matsumoto et al. [200]. They simulated the interaction force of an edge dislocation with segregated H under various dislocation velocities, reporting that H exerts a significant dragging or pinning force of more than 500 MPa in shear stress. Notably, the H concentration assumed in their study was less than the equilibrium in an H_2 gas environment with an atmospheric pressure. Their companion analysis also inferred that the accelerated dislocation motion observed in TEM is an artifact stemming from the adsorption of H atoms on the surface of thin foils [209].

In terms of a small-sized mechanical test in an environmental SEM, the research group of Barnoush et al. has recently proposed a new H-assisted cracking mechanism in an assumption opposed to the well-accepted localized plasticity concept [193,210]. Since the H-induced crack acceleration in Fe–Al intermetallic alloy accompanies a restricted extension of the crack-tip plasticity, they claimed that accumulated H atoms into the crack-tip critically decrease the dislocation mobility. Crucially, this idea is compatible with the recent computational simulations mentioned above [198,200,201,206]. Thanks to the fracture model by Barnoush et al., the authors finally consider the most plausible crack propagation mechanism for Stage B as follows.

The dislocations, which are emitted from the crack-tip, are promptly immobilized by locally accumulated H atoms. Considering the crack-tip zone where dilatational hydrostatic stress, σ_h, becomes significant, such stress-dependent H accumulation obeys the Arrhenius-type statistical equation in the simplest form [20,33].

$$C_{\mathrm{H,local}} = C_0 \exp\left(\frac{\sigma_{\mathrm{h}} V_{\mathrm{H}}}{R_{\mathrm{U}} T}\right) \tag{4}$$

where C_0 is the thermal equilibrium H concentration under zero stress, and V_H is the molar volume of H in iron. Because of the restricted dislocation movement, crack-tip blunting and associated local stress relief (*i.e.*, plastic relaxation) become infeasible. The stress shielding by emitted dislocations [190] is also weakened accordingly, increasing the local stress far beyond that under the absence of H. With the aid of these stress-amplifying factors, crack propagation commences when a critical crack-tip stress is reached under an increase in the externally applied load. The propagation process may involve an initiation of a precursory micro-crack at the location with maximum hydrostatic stress ahead of the main crack-tip and its coalescence with the main crack. This precursory micro-crack potentially nucleates along {001} cleavage plane [74,146,211]. Or otherwise, they are along specific crystallographic planes such as {011} [55,113,148], wherein atomistic cohesive energy could more or less be reduced by H [155,212]. Ultimately, the crack is temporarily arrested after passing through this extremely stressed and H-accumulated zone. These series of events are repeated in cycle-by-cycle.

The brittle-like striation on the CIT surface (Fig. 9) may be a consequence of small crack-tip blunting *via* the emission of a small number of dislocations or the temporal crack arrest. In terms of the nucleation of precursory micro-crack ahead of the main crack, our model is positioned in-between the models by Marrow (Fig. 18 (b)) and Nishikawa (Fig. 18 (d)). Nonetheless, the essence of our model is entirely different from these two previous models. We consistently assume H-induced locking of dislocations rather than mere lattice decohesion or enhanced dislocation mobility.

The locking of dislocations at the crack-tip may also be caused by other interstitial elements like carbon or nitrogen. Nevertheless, the solubility of these elements in BCC iron is quite low at around room temperature (*e.g.*, for carbon, it is less than 1 mass ppm), besides their diffusion is much slower than H. Thus, long-range diffusion is required for their accumulation into the hydrostatic stress field around the crack-tip, which is not feasible within the time scale of one loading cycle in the FCG test. Regarding H, it would also require a decent time duration if H was pre-charged (not supplied from the gaseous phase) and needed to accumulate into the crack-tip *via* diffusion through the iron lattice. Indeed, in ferrite-pearlite carbon steel containing ≈1 mass ppm pre-charged H after immersion into NH_4SCN, the FCG acceleration was observed only at a low loading frequency of less than 0.1 Hz [213]. Since H is continuously supplied from the proximity of the crack-tip fracture process zone, a gaseous H_2 environment is deemed to be the most severe practical condition for the emergence of HA-FCG. Such a direct atom supply into the crack-tip can be achieved for other interstitial elements if one uses special experimental equipment. Narita et al. performed static crack growth tests of Fe-2.5%Si ferritic single crystals under gaseous plasmas of 25 Pa hydrogen, helium, and nitrogen [214]. They reported accelerated crack growth without crack-tip blunting not only by H but also by He. Even by N, brittle crack propagation can be observed at 450 K where N diffusivity becomes considerable. The mechanism proposed in this paper may be relevant to these embrittlement phenomena caused by other right elements, motivating us to further verify such universality of our dislocation locking model.

4.3.4. *Conformity to the phenomenological findings*

The model established in Section 4.3.3 tentatively relies on two primary assumptions: H-induced locking of dislocations in the crack-tip zone; and H-induced reduction of interatomic cohesive energy along some specific crystallographic planes. Both the significance of dislocation immobilization and the easiness of atomistic plane separation should be H-concentration-dependent. For the onset of Stage B, the combination of those two factors and the externally applied stress must reach a certain criterion, which is sufficient to encompass the CIT crack growth. Such a simple hypothesis likely leads to qualitative but plausible explanations for the presence of Stage A-to-B transition and its dependency on the H_2 gas pressure (Fig. 4 (a)). In what follows, the validity of our new model is examined in light of some supporting experimental information.

According to Eq. (4), an increase in ΔK leads to a greater H accumulation into the crack-tip zone *via* an increase in σ_h. This increasing local H concentration eventually renders the decreasing dislocation mobility and the reduction in atomistic cohesive energy both effective. In addition, an increase in applied load escalates the driving force for fracture, *i.e.*, normal stress to the crack plane. When these multiple factors compositely reach a criterion under an increasing ΔK, CIT crack growth overwhelms IG and triggers the HA-FCG transition from Stage A to B. As the H_2 gas pressure becomes higher and the local crack-tip H concentration accordingly increases, such a criterion should readily be reached even under a smaller ΔK. This is the potential reason why the Stage A-to-B transition shifts to smaller ΔK with an increase in the H_2 gas pressure (Fig. 4 (a)). Here, let us approximate that the criterion for the emergence of CIT is almost bipolarized: whether the applied stress and an H-induced decrease in dislocation mobility (*i.e.*, restriction of plastic relaxation) are sufficient enough to cleave the lattice or not. In this regard, it seems reasonable that the FCG acceleration rate in Stage B shows only a weak dependency on H_2 gas pressure once after the acceleration started (Fig. 5 (a)), while ΔK for the onset of Stage B is strongly pressure-dependent (Fig. 4). To say conversely, such a weak dependency on H_2 gas pressure implies greater importance of dislocation immobilization than the reduction in atomistic cohesion for the CIT fracture.

The dependencies of the Stage B FCG acceleration rate on temperature and loading frequency (Fig. 4 (b) and Fig. 5 (b)) can also be rationalized by the new model. One should consider the thermal equilibrium state of H-trapping by dislocation, as well as the thermal activation process of the dislocation to overcome those segregated H. At an elevated temperature, the thermal vibration of H atoms is substantial, and thereby H tends to evaporate from the dislocation's trapping. Thus, H-induced immobilization of crack-tip dislocations is no longer operational. The occupancy of H atoms around dislocation lines also follows the Fermi-Dirac formula of Eq. (3) [179]. Matsuoka et al. systematically studied the relationship between θ_x and the dependencies of Stage B FCG acceleration rate on the H_2 gas pressure and temperature like Fig. 17. They reported that $E_b = 47$ kJ/mol yields the best fit of their experimental data [72]. Indeed, this value of E_b is closely correlated with the analytically determined binding energy between an H atom and a region close to the dislocation core in iron [215]. Moreover, it is also a thermal activation process for a dislocation to move forward *via* overcoming or dragging the obstacle solute atoms segregated in the dislocation core [216,217]. Assuming an extreme condition where dislocation velocity is significantly faster than solute diffusion, the probability of dislocation segment with the length, l_{crit}, for surmounting the obstacles *via* Fisher-type breakaway [218] has been formulated by Lothe [217].

$$P_{breakaway} = \left(\frac{1}{C_0}\right)^{l_{crit}/b} \exp\left(-\frac{l_{crit}E_{B,disl}}{bR_U T}\right) \tag{5}$$

where b is the magnitude of Burgers vector, and $E_{B,disl}$ is the interaction energy of H atoms with the dislocation. Namely, an increase in temperature synergistically aids the movement of dislocation not only by reducing the local H concentration along the dislocation line (Eq. (3)) but also by an exponential increase in $P_{breakaway}$. Besides, with the decrease in local strain rate inside the crack-tip zone (*i.e.*, decreasing loading frequency), there would be more chance for the dislocation to surmount the obstacle H atoms even under the same local H concentration and temperature. That is, the dislocations, which have been immobile under a relatively fast loading frequency, can theoretically be mobilized *via* thermally activated overcoming of obstacles as the loading rate decreases.

Note that Eq. (5) seems inapplicable to the case where dislocation velocity and H diffusivity are competitive. Under such a circumstance, H primarily exerts the atmosphere drag resistance. Nonetheless, such dragging motion requires successive short-range jumps of individual H atoms toward the direction of dislocation movement, which can also be regarded as a framework of breakaway events on an atomic scale. The feasibility for this type of motion is also expressed by an Arrhenius form like Eq. (5) [200,219], including the binding energy of H and the H concentration along the dislocation line in the numerator of the exponent. Thus, the universality of Eq. (5) can express both types of dislocation motion *via* solute drag and atmosphere breakaway.

Most recently, the two of the present authors tried to formulate the temperature- and loading rate-dependencies of HA-FCG by implementing both the thermal equilibrium of H-trapping state in dislocations and thermally activated overcome (drag or breakaway) of dislocations from the H atoms along their core [220]. We employed Eq. (3) for expressing the former, while the latter was taken into account by a simplified Arrhenius form as the following Eq. (6). The simplest form of an equation for the FCG rate is given by Eq. (7).

$$P_{break} = \exp\left(-\frac{C_1 E_B \theta_x}{R_U T}\right) \tag{6}$$

$$\left(\frac{da}{dN}\right)_H = (1 - P_{break})^{C_2/f}\left\{\left(\frac{da}{dN}\right)_{H,max} - \left(\frac{da}{dN}\right)_N\right\} + \left(\frac{da}{dN}\right)_N \tag{7}$$

where $(da/dN)_{H,max}$ is the upper limit of FCG rate in H_2 gas. C_1 and C_2 are fitting constants.

Fig. 19 shows the loading frequency-dependencies of the magnitudes of HA-FCG in a 0.16% carbon steel under 0.7 MPa H_2 gas at $\Delta K = 30$ MPa $m^{1/2}$ (*i.e.*, Stage B regime) for various temperatures of 300~423 K. The fitting results with Eq. (7) are drawn with solid curves, wherein their good correspondence with the experimental data is evident. For any sake, the success of Eq. (7) in expressing the practical HA-FCG behavior substantiates our concept: a predominant responsibility of H-induced obstruction of dislocation motion at the crack-tip. In reality, drag resistance and pinning force competitively operate, the latter of which may become increasingly important and lead to more substantial FCG acceleration at a lower temperature and faster loading frequency.

5. Summary and remaining tasks

Our series of experimental studies and literature survey substantiated an explicit manifestation of the hydrogen-assisted fatigue crack growth (HA-FCG) in ferritic iron and steels comprising Stage A, which predominates at a low ΔK domain below ≈15 MPa $m^{1/2}$, and Stage B at a higher ΔK. These two stages were distinct in their microscale fracture surfaces and crystallographic cracking pathways, macroscopically leading to the critical difference in the corresponding FCG acceleration

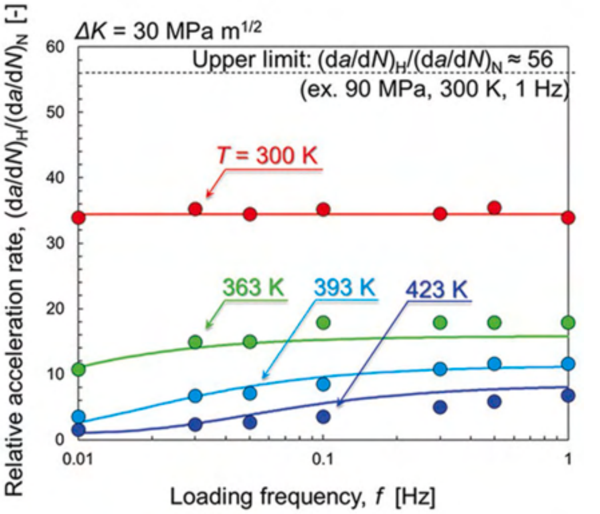

Fig. 19. Loading frequency-dependence of the HA-FCG in a 0.16% low-carbon steel under 0.7 MPa H_2 gas at $\Delta K = 30$ MPa $m^{1/2}$ for various temperatures of 300∼423 K [220]. The circle plots display the experimentally acquired data, while solid lines are the results of data fitting with Eq. (7).

rate. This dual-stage HA-FCG is schematically summarized in Fig. 20, wherein brief descriptions of the dependencies on mechanistic and environmental variables, as well as prevailing failure mechanisms in each stage, are appended.

The main failure mode in Stage A is intergranular (IG), the propensity (*i.e.*, area fraction on the fracture surface) of which increases with an increase in H_2 gas pressure. However, the nature of this IG is entirely different from the brittle IG usually reported in the HE of high-strength materials [33,104,107]. Its key process is micro-void nucleation and coalescence along the grain boundaries (GBs) involved within the cyclically deformed plastic zone (CPZ) ahead of the crack-tip *via* some forms of H-GB-dislocation interactions (Fig. 20 (b)). Accordingly, the final separation of GBs inherently requires an accumulation of plastic strain inside the CPZ with the aid of cyclic loading. Owing to this requirement for cyclic plasticity and concomitant energy dissipation, the FCG acceleration rate in Stage A remains relatively mild (up to 10 times). Considering that a major part of fatigue life in real industrial components is consumed by FCG at a low-stress intensity range, the presence of this mild acceleration regime is practically desirable for ensuring the material's robustness under a defect-tolerant design.

Meanwhile, substantial FCG acceleration up to 100 times occurs in Stage B. The fracture surface is replaced entirely with a transgranular mode accompanying brittle-like striations, which has conventionally been termed quasi-cleavage (QC) [42,73,116]. However, such transgranular fracture is a consequence of the crack propagation partly along {001} cleavage plane, thereby designated in the present paper as "*cleavage-involving transgranular (CIT)*" cracking (Fig. 20 (c)). What should be emphasized is a dramatic reduction of the plasticity development around the crack-wake, which is distinct from the plasticity-mediated IG HA-FCG in Stage A. Although an increasing H_2 gas pressure renders the critical ΔK for Stage A-to-B transition smaller, the FCG acceleration rate in Stage B is rather pressure-insensitive. A plausible model to rationalize such pressure independence is the immobilization of dislocations and an inhibited stress relief at the crack-tip, which has recently been proposed [193,210] in opposition to the well-accepted H-enhanced localized plasticity models [142,185,183]. In this context, a prompt increase in the FCG acceleration rate at the Stage A-to-B transition seems reasonable because the essential failure mode suddenly changes from plasticity-mediated to locally brittle. Note however that the CIT facets involved minute undulations even in the regions in-between the lines of brittle-like striation as can be seen in Figs. 9 and 14 (i), a feature different from the conventional cleavage fracture that is almost perfectly flat [221]. One possible reason for such configurational complexity is the plastic deformation preliminarily introduced within the CPZ, possibly encompassing some curvatures of the crystal planes prior to fracture. Additionally, the emission of a small number of dislocations that will eventually be immobilized by H or the arresting process of the crack after the passage of the locally brittle zone (*i.e.*, the formation process of brittle-like striation lines) also the potential causes of minute crack-tip plasticity, which are not the case in ordinary cleavage.

It is crucial to state again that, in both Stages A and B, the prerequisite for IG and CIT fractures is the significance of H-trapping by defects: GBs for Stage A and dislocations for Stage B. Due to the

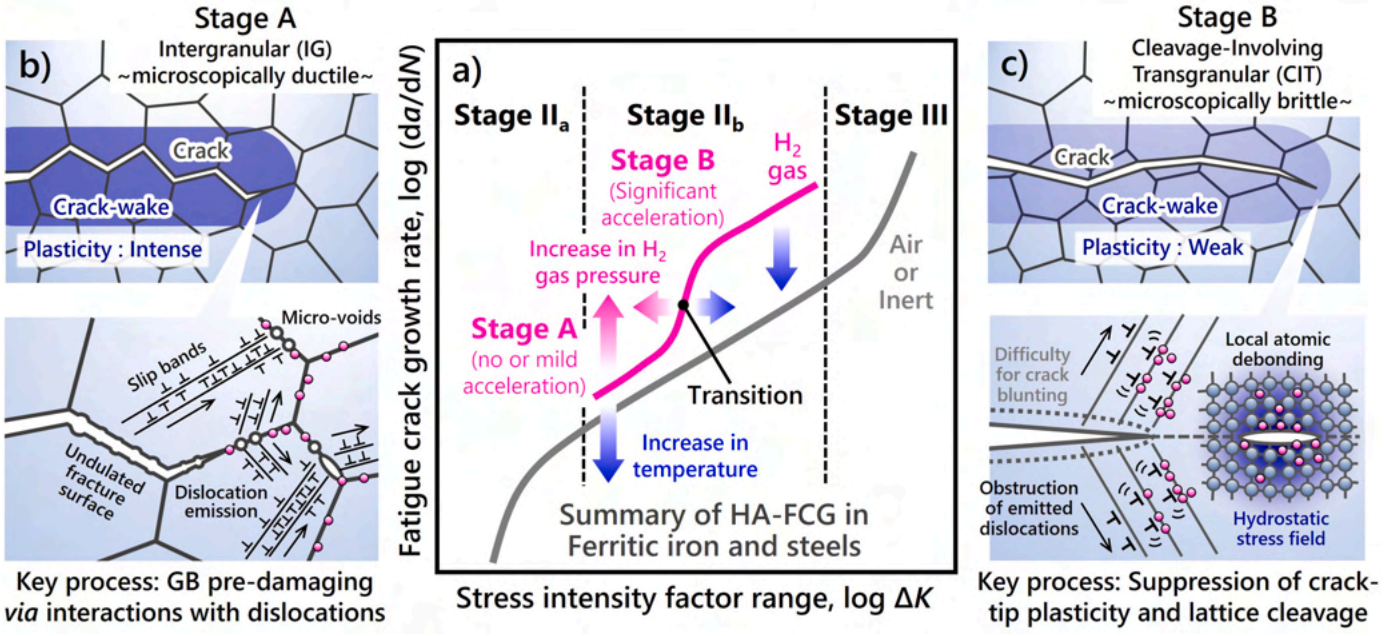

Fig. 20. Summary of the HA-FCG behavior in ferritic iron and steels. (a) da/dN-ΔK curve consisting of dual stages A and B, (b) processes of intergranular (IG) crack propagation in Stage A, and (c) potential mechanism of *cleavage-involving transgranular (CIT)*, *i.e.*, conventionally called quasi-cleavage, fracture in Stage B.

exponential temperature dependence of the trap site H-occupancies (Eq. (3)), an increase in temperature consistently mitigates the FCG acceleration in both stages and shifts the Stage A-to-B transition toward a higher ΔK.

While this overview provided our latest understanding, some unresolved assignments remain to be cleared up. The typical issue is the further details of the crack path crystallography in Stage B. The fracture model in Fig. 20 (c) was established based on the authors' finding of {001}-type crack propagation. However, this {001}-type HE fracture has not necessarily been observed even in the HE of similar bcc-based steels [110,113,122]. One possible reason for this contradiction is the differences in stress state depending on the specimen configurations. The authors' observations were all performed at the mid-thickness portion of the CT specimen with $B = 10$ mm, where the plane-strain stress state prevails [222]. Under such a circumstance, cleavage-type brittle fracture is more likely to emerge compared to thinner specimens due to high-stress triaxiality and resultant plasticity constraint [222,223]. To tackle this point, clarification of the effect of sample thickness and additional analyses of statistically significant numbers of grains are required. Moreover, preferential crack propagation along other crystallographic planes such as {011} under higher H_2 gas pressure is also a mystery. Elaborations on these assignments will give us a more advanced and complete form of Fig. 20 (c).

From the practical point of view, HA-FCG data at lower (below ambient) temperatures, as well as systematic elucidations of the influences of load ratio and microstructural variables, are also essential. Hopefully, it will be valuable for the life assessment of engineering components if one can quantitatively estimate the Stage A-to-B transition as a function of ΔK, R, f, temperature, and H_2 gas pressure. Several modeling works have been carried out to formulate the onset of Stage B [20,45,224], and seemingly have reached an apparent success. Nevertheless, the implemented parameters in their formulae are, although these are indeed vital, only the H-diffusion/accumulation kinetics and CPZ size. A standpoint on the changes in fractographic characters is still lacking. Finally, a motivation from our discoveries (*i.e.*, microstructure- and crystallography-dependent crack propagation) is to modify the microstructure *via* adequate thermo-mechanical processing. This has not been directed in the field of FCG in steels because of the fair microstructural insusceptibility of Stage II da/dN-ΔK curves in air and inert environments. By optimizing, for instance, grain size, GB characters, and rolling textures along the principal stress axis, an innovative ferritic steel with a lowered sensitivity to HA-FCG can potentially be created. Proactive efforts in addressing these challenges should advance both the development of novel H-compatible structural materials and consequent enhancement in the reliability of H energy-related devices.

CRediT authorship contribution statement

Yuhei Ogawa: Writing – original draft, Investigation, Conceptualization. **Osamu Takakuwa:** Writing – review & editing, Validation, Investigation, Conceptualization. **Akinobu Shibata:** Writing – review & editing, Validation, Supervision.

Declaration of competing interest

The authors declare that they have no known competing financial interests or personal relationships that could have appeared to influence the work reported in this paper.

Acknowledgments

The experimental works included in this overview were partially supported by JSPS KAKENHI (Grant numbers 19K23503 and 20K04161). Some parts of the presented FCG data were acquired in the Research Center for Hydrogen Industrial Use and Storage (HYDROGENIUS) during Y.O.'s tenure at Kyushu University, where he was previously affiliated (now affiliated with NIMS). Dr. Domas Birenis, a former Ph.D. student at the University of Oslo, is greatly acknowledged for his contribution to our TEM observations.

References

[1] Quakernaat J. Hydrogen in a global long-term perspective. Int J Hydrogen Energy 1995;20:485–92. https://doi.org/10.1016/0360-3199(94)00078-E.

[2] Bockris J. Hydrogen no longer a high cost solution to global warming: new ideas. Int J Hydrogen Energy 2008;33:2129–31. https://doi.org/10.1016/j.ijhydene.2008.02.030.

[3] Acar C, Dincer I. The potential role of hydrogen as a sustainable transportation fuel to combat global warming. Int J Hydrogen Energy 2020;45:3396–406. https://doi.org/10.1016/j.ijhydene.2018.10.149.

[4] Itaoka K, Saito A, Sasaki K. Public perception on hydrogen infrastructure in Japan: influence of rollout of commercial fuel cell vehicles. Int J Hydrogen Energy 2017;42:7290–6. https://doi.org/10.1016/j.ijhydene.2016.10.123.

[5] Kurtz J, Sprik S, Bradley TH. Review of transportation hydrogen infrastructure performance and reliability. Int J Hydrogen Energy 2019;44:12010–23. https://doi.org/10.1016/j.ijhydene.2019.03.027.

[6] Barthélémy H. Hydrogen storage – industrial prospectives. Int J Hydrogen Energy 2012;37:17364–72. https://doi.org/10.1016/j.ijhydene.2012.04.121.

[7] Samuelsen S, Shaffer B, Grigg J, Lane B, Reed J. Performance of a hydrogen refueling station in the early years of commercial fuel cell vehicle deployment. Int J Hydrogen Energy 2020;45:31341–52. https://doi.org/10.1016/j.ijhydene.2020.08.251.

[8] Faye O, Szpunar J, Eduok U. A critical review on the current technologies for the generation, storage, and transportation of hydrogen. Int J Hydrogen Energy 2022;47:13771–802. https://doi.org/10.1016/j.ijhydene.2022.02.112.

[9] Louthan MR, Caskey GR, Donovan JA, Rawl DE. Hydrogen embrittlement of metals. Mater Sci Eng 1972;10:357–68. https://doi.org/10.1016/0025-5416(72)90109-7.

[10] Bhadeshia HKDH. Prevention of hydrogen embrittlement in steels. ISIJ Int 2016;56:24–36. https://doi.org/10.2355/isijinternational.ISIJINT-2015-430.

[11] Djukic MB, Bakic GM, Zeravcic VS, Sedmak A, Rajicic B. Hydrogen embrittlement of industrial components: prediction, prevention, and models. Corrosion 2016;72:943–61. https://doi.org/10.5006/1958.

[12] Hirth JP. Effects of hydrogen on the properties of iron and steel. Metall Trans A 1980;11:861–90. https://doi.org/10.1007/BF02654700.

[13] Johnson WH. On some remarkable changes produced in iron and steel by the action of hydrogen and acids. Proc Roy Soc Lond 1875;23:168–79. https://doi.org/10.1098/rspl.1874.0024.

[14] Briottet L, Moro I, Escot M, Furtado J, Bortot P, Tamponi GM, Solin J, Odemer G, Blanc C, Andrieu E. Fatigue crack initiation and growth in a CrMo steel under hydrogen pressure. Int J Hydrogen Energy 2015;40:17021–30. https://doi.org/10.1016/j.ijhydene.2015.05.080.

[15] Macadre A, Artamonov M, Matsuoka S, Furtado J. Effects of hydrogen pressure and test frequency on fatigue crack growth properties of Ni-Cr-Mo steel candidate for a storage cylinder of a 70MPa hydrogen filling station. Eng Fract Mech 2011;78:3196–211. https://doi.org/10.1016/j.engfracmech.2011.09.007.

[16] Yamabe J, Itoga H, Awane T, Matsuo T, Matsunaga H, Matsuoka S. Pressure cycle testing of Cr–Mo steel pressure vessels subjected to gaseous hydrogen. J Pressure Vessel Technol 2016;138. https://doi.org/10.1115/1.4030086.

[17] Yamabe J, Awane T, Matsuoka S. Investigation of hydrogen transport behavior of various low-alloy steels with high-pressure hydrogen gas. Int J Hydrogen Energy 2015;40:11075–86. https://doi.org/10.1016/j.ijhydene.2015.07.006.

[18] Haeseldonckx D, Dhaeseleer W. The use of the natural-gas pipeline infrastructure for hydrogen transport in a changing market structure. Int J Hydrogen Energy 2007;32:1381–6. https://doi.org/10.1016/j.ijhydene.2006.10.018.

[19] Cerniauskas S, Jose Chavez Junco A, Grube T, Robinius M, Stolten D. Options of natural gas pipeline reassignment for hydrogen: cost assessment for a Germany case study. Int J Hydrogen Energy 2020;45:12095–107. https://doi.org/10.1016/j.ijhydene.2020.02.121.

[20] Amaro RL, Rustagi N, Findley KO, Drexler ES, Slifka AJ. Modeling the fatigue crack growth of X100 pipeline steel in gaseous hydrogen. Int J Fatig 2014;59:262–71. https://doi.org/10.1016/j.ijfatigue.2013.08.010.

[21] Kappes MA, Perez T. Hydrogen blending in existing natural gas transmission pipelines: a review of hydrogen embrittlement, governing codes, and life prediction methods. Corrosion Rev 2023;41:319–47. https://doi.org/10.1515/corrrev-2022-0083.

[22] Ustolin F, Paltrinieri N, Berto F. Loss of integrity of hydrogen technologies: a critical review. Int J Hydrogen Energy 2020;45:23809–40. https://doi.org/10.1016/j.ijhydene.2020.06.021.

[23] Lynch S. Hydrogen embrittlement phenomena and mechanisms. Corrosion Rev 2012;30:105–23. https://doi.org/10.1515/corrrev-2012-0502.

[24] Takakuwa O, Yamabe J, Matsunaga H, Furuya Y, Matsuoka S. Comprehensive understanding of ductility loss mechanisms in various steels with external and internal hydrogen. Metall Mater Trans A Phys Metall Mater Sci 2017;48:5717–32. https://doi.org/10.1007/s11661-017-4323-3.

[25] NASA. Safety standard for hydrogen and hydrogen systems. Washington, DC. 1997. NSS1740.16.

[26] San Marchi C, Somerday BP. Technical reference for hydrogen compatibility of materials. http://www.ntis.gov/help/ordermethods.asp?loc=7-4-0#online; 2012.

[27] Michler T, Naumann J. Microstructural aspects upon hydrogen environment embrittlement of various bcc steels. Int J Hydrogen Energy 2010;35:821–32. https://doi.org/10.1016/j.ijhydene.2009.10.092.

[28] Cho L, Bradley PE, Lauria DS, Connolly MJ, Seo EJ, Findley KO, Speer JG, Golem L, Slifka AJ. Effects of hydrogen pressure and prior austenite grain size on the hydrogen embrittlement characteristics of a press-hardened martensitic steel. Int J Hydrogen Energy 2021;46:24425–39. https://doi.org/10.1016/j.ijhydene.2021.05.005.

[29] Nibur KA, Somerday BP, Marchi CS, Foulk JW, Dadfarnia M, Sofronis P. The relationship between crack-tip strain and subcritical cracking thresholds for steels in high-pressure hydrogen gas. Metall Mater Trans 2012;44:248–69. https://doi.org/10.1007/s11661-012-1400-5.

[30] Komoda R, Kubota M, Staykov A, Ginet P, Barbier F, Furtado J. Inhibitory effect of oxygen on hydrogen-induced fracture of A333 pipe steel. Fatig Fract Eng Mater Struct 2019;42:1387–401. https://doi.org/10.1111/ffe.12994.

[31] Barthélémy H. Effects of pressure and purity on the hydrogen embrittlement of steels. Int J Hydrogen Energy 2011;36:2750–8. https://doi.org/10.1016/j.ijhydene.2010.05.029.

[32] Gangloff RP. Hydrogen-assisted cracking. In: Comprehensive structural integrity. Elsevier; 2003. p. 31–101. https://doi.org/10.1016/B0-08-043749-4/06134-6.

[33] McMahon CJ. Hydrogen-induced intergranular fracture of steels. Eng Fract Mech 2001;68:773–88. https://doi.org/10.1016/S0013-7944(00)00124-7.

[34] Uyama H, Nakashima M, Morishige K, Mine Y, Murakami Y. Effects of hydrogen charge on microscopic fatigue behaviour of annealed carbon steels. Fatig Fract Eng Mater Struct 2006;29:1066–74. https://doi.org/10.1111/j.1460-2695.2006.01069.x.

[35] Ogawa Y, Matsunaga H, Yamabe J, Yoshikawa M, Matsuoka S. Unified evaluation of hydrogen-induced crack growth in fatigue tests and fracture toughness tests of a carbon steel. Int J Fatig 2017;103:223–33. https://doi.org/10.1016/j.ijfatigue.2017.06.006.

[36] Yamabe J, Matsunaga H, Furuya Y, Hamada S, Itoga H, Yoshikawa M, Takeuchi E, Matsuoka S. Qualification of chromium-molybdenum steel based on the safety factor multiplier method in CHMC1-2014. Int J Hydrogen Energy 2015;40:719–28. https://doi.org/10.1016/j.ijhydene.2014.10.114.

[37] Smirnova D, Starikov S. Atomistic study of hydrogen diffusion in presence of defects in bcc and fcc iron. Comput Mater Sci 2023;230. https://doi.org/10.1016/j.commatsci.2023.112433.

[38] Kumnick aJ, Johnson HH. Hydrogen transport through annealed and deformed armco iron. Metall Trans A 1974;5:1199–206. https://doi.org/10.1007/BF02644334.

[39] San Marchi C, Somerday B, Robinson S. Permeability, solubility and diffusivity of hydrogen isotopes in stainless steels at high gas pressures. Int J Hydrogen Energy 2007;32:100–16. https://doi.org/10.1016/j.ijhydene.2006.05.008.

[40] Kanezaki T, Narazaki C, Mine Y, Matsuoka S, Murakami Y. Effects of hydrogen on fatigue crack growth behavior of austenitic stainless steels. Int J Hydrogen Energy 2008;33:2604–19. https://doi.org/10.1016/j.ijhydene.2008.02.067.

[41] Cotterill PJ, King JE. Hydrogen embrittlement contributions to fatigue crack growth in a structural steel. Int J Fatig 1991;13:447–52. https://doi.org/10.1016/0142-1123(91)90478-H.

[42] Cialone HJ, Holbrook JH. Effects of gaseous hydrogen on fatigue crack growth in pipeline steel. Metall Trans A 1985;16:115–22. https://doi.org/10.1007/BF02656719.

[43] Slifka AJ, Drexler ES, Nanninga NE, Levy YS, McColskey JD, Amaro RL, Stevenson AE. Fatigue crack growth of two pipeline steels in a pressurized hydrogen environment. Corrosion Sci 2014;78:313–21. https://doi.org/10.1016/j.corsci.2013.10.014.

[44] Somerday BP, Sofronis P, Nibur KA, San Marchi C, Kirchheim R. Elucidating the variables affecting accelerated fatigue crack growth of steels in hydrogen gas with low oxygen concentrations. Acta Mater 2013;61:6153–70. https://doi.org/10.1016/j.actamat.2013.07.001.

[45] Yamabe J, Yoshikawa M, Matsunaga H, Matsuoka S. Hydrogen trapping and fatigue crack growth property of low-carbon steel in hydrogen-gas environment. Int J Fatig 2017;102:202–13. https://doi.org/10.1016/j.ijfatigue.2017.04.010.

[46] Ogawa Y, Iwata K. Resistance of pearlite against hydrogen-assisted fatigue crack growth. Int J Hydrogen Energy 2022;47:31703–8. https://doi.org/10.1016/j.ijhydene.2022.07.074.

[47] Krauss G. Steels -processing, structure, and performances. second ed. Materials Park, Ohio: ASM International; 2015.

[48] Abbaschian R, Abbaschian L. Physical metallurgy principles. fourth ed. Cl-Engineering; 2008.

[49] Ritchie RO. Near-threshold fatigue-crack propagation in steels. Int Met Rev 1979;24:205–30. https://doi.org/10.1179/imtr.1979.24.1.205.

[50] Richards CE, Lindley TC. The influence of stress intensity and microstructure on fatigue crack propagation in ferritic materials. Eng Fract Mech 1972;4:951–78. https://doi.org/10.1016/0013-7944(72)90028-8.

[51] Sadananda K, Vasudevan AK. Fatigue crack growth mechanisms in steels. Int J Fatig 2003;25:899–914. https://doi.org/10.1016/S0142-1123(03)00128-2.

[52] Nanninga N, Slifka A, Levy Y, White C. A review of fatigue crack growth for pipeline steels exposed to hydrogen. J Res Natl Inst Stand Technol 2010;115:437. https://doi.org/10.6028/jres.115.030.

[53] Ronevich JA, Somerday BP, San Marchi CW. Effects of microstructure banding on hydrogen assisted fatigue crack growth in X65 pipeline steels. Int J Fatig 2015;82:497–504. https://doi.org/10.1016/j.ijfatigue.2015.09.004.

[54] Ogawa Y, Iwata K. Fatigue crack propagation in pearlitic steel under pressurized gaseous hydrogen: influences of microstructure size and strength level. ISIJ Int 2023. https://doi.org/10.2355/isijinternational.ISIJINT-2023-011. ISIJINT-2023-011.

[55] Ogawa Y, Nishida H, Nakamura M, Olden V, Vinogradov A, Matsunaga H. Dual roles of pearlite microstructure to interfere/facilitate gaseous hydrogen-assisted fatigue crack growth in plain carbon steels. Int J Fatig 2022;154:106561. https://doi.org/10.1016/j.ijfatigue.2021.106561.

[56] Matsuoka S, Matsunaga H, Yamabe J, Hamada S, Iijima T. Various strength properties of SCM435 and SNCM439 low-alloy steels in 115 MPa hydrogen gas and proposal of design guideline. Transactions of the JSME 2017;83. https://doi.org/10.1299/transjsme.17-00264.

[57] Ogawa Y, Kuriyama K, Koyama M. Dual grain size-effects on hydrogen-assisted fatigue crack growth in 1 GPa-class medium-carbon martensitic steel. Int J Hydrogen Energy 2023. https://doi.org/10.1016/j.ijhydene.2023.08.317.

[58] Lynch S. Some fractographic contributions to understanding fatigue crack growth. Int J Fatig 2017. https://doi.org/10.1016/j.ijfatigue.2017.06.036.

[59] Marrow TJ, Cotterill PJ, King JE. Temperature effects on the mechanism of time independent hydrogen assisted fatigue crack propagation in steels. Acta Metall Mater 1992;40:2059–68. https://doi.org/10.1016/0956-7151(92)90192-H.

[60] Drexler ES, Slifka AJ, Amaro RL, Barbosa N, Lauria DS, Hayden LE, Stalheim DG. Fatigue crack growth rates of API X70 pipeline steel in a pressurized hydrogen gas environment. Fatig Fract Eng Mater Struct 2014;37:517–25. https://doi.org/10.1111/ffe.12133.

[61] Brazill R, Simmons GW, Wei RP. Fatigue crack growth in 2-1/4-Cr-1Mo steel exposed to hydrogen containing gases. J Eng Mater Technol 1979;101:199–204. https://doi.org/10.1115/1.3443678.

[62] Austen IM, Mcintyre P. Corrosion fatigue of high-strength steel in low-pressure hydrogen gas. Met Sci 1979;13:420–8. https://doi.org/10.1179/msc.1979.13.7.420.

[63] Sun Z, Benoit G, Moriconi C, Hamon F, Halm D, Hamon F, Hénaff G. Fatigue crack propagation under gaseous hydrogen in a precipitation-hardened martensitic stainless steel. Int J Hydrogen Energy 2011;36:8641–4. https://doi.org/10.1016/j.ijhydene.2011.04.094.

[64] Yamabe J, Matsumoto T, Matsuoka S, Murakami Y. A new mechanism in hydrogen-enhanced fatigue crack growth behavior of a 1900-MPa-class high-strength steel. Int J Fract 2012;177:141–62. https://doi.org/10.1007/s10704-012-9760-9.

[65] Setoyama A, Ogawa Y, Nakamura M, Tanaka Y, Chen T, Koyama M, Matsunaga H. Transition mechanism of cycle- to time-dependent acceleration of fatigue crack-growth in 0.4 %C Cr-Mo steel in a pressurized gaseous hydrogen environment. Int J Fatig 2022;163:107039. https://doi.org/10.1016/j.ijfatigue.2022.107039.

[66] Wachob HF, Nelson HG. Influence of microstructure on the fatigue crack growth of A516 in hydrogen. In: Proceedings of the third international conference on effect of hydrogen on behavior of materials; 1980. p. 703–11. Moran, WY, USA.

[67] Suresh S, Ritchie RO. Mechanistic dissimilarities between environmentally influenced fatigue-crack propagation at near-threshold and higher growth rates in lower strength steels. Met Sci 1982;16:529–38. https://doi.org/10.1179/msc.1982.16.11.529.

[68] Fukuyama S, Han G, He J, Yokogawa K. Effect of high pressure hydrogen gas on crack growth of carbon steel. J Soc Mater Sci Japan 1997;46:607–12. https://doi.org/10.2472/jsms.46.607.

[69] San Marchi C, Somerday BP, Nibur KA, Stalheim DG, Boggess T, Jansto S. Fracture resistance and fatigue crack growth of X80 pipeline steel in gaseous hydrogen. Mater Fabrica Parts A B 2011;6:841–9. https://doi.org/10.1115/PVP2011-57684. ASMEDC.

[70] Nishikawa H, Oda Y, Noguchi H. Loading-frequency effects on fatigue crack growth behavior of a low carbon steel JIS S10C in hydrogen gas environment. J Solid Mech Mater Eng 2011;5:104–16. https://doi.org/10.1299/jmmp.5.104.

[71] Koyama M, Onishi Y, Noguchi H. Characteristics of hydrogen-assisted intergranular fatigue crack growth in interstitial-free steel: role of plastic strain localization. Int J Fract 2017;206:123–30. https://doi.org/10.1007/s10704-017-0205-3.

[72] Matsuoka S, Takakuwa O, Okazaki S, Yoshikawa M, Yamabe J, Matsunaga H. Peculiar temperature dependence of hydrogen-enhanced fatigue crack growth of low-carbon steel in gaseous hydrogen. Scripta Mater 2018;154:101–5. https://doi.org/10.1016/j.scriptamat.2018.05.035.

[73] Wang S, Nagao A, Sofronis P, Robertson IM. Hydrogen-modified dislocation structures in a cyclically deformed ferritic-pearlitic low carbon steel. Acta Mater 2018;144:164–76. https://doi.org/10.1016/j.actamat.2017.10.034.

[74] Birenis D, Ogawa Y, Matsunaga H, Takakuwa O, Yamabe J, Prytz Ø, Thøgersen A. Interpretation of hydrogen-assisted fatigue crack propagation in BCC iron based on dislocation structure evolution around the crack wake. Acta Mater 2018;156:245–53. https://doi.org/10.1016/j.actamat.2018.06.041.

[75] Shinko T, Hénaff G, Halm D, Benoit G, Bilotta G, Arzaghi M. Hydrogen-affected fatigue crack propagation at various loading frequencies and gaseous hydrogen pressures in commercially pure iron. Int J Fatig 2019;121:197–207. https://doi.org/10.1016/j.ijfatigue.2018.12.009.

[76] Ogawa Y, Birenis D, Matsunaga H, Thøgersen A, Prytz Ø, Takakuwa O, Yamabe J. Multi-scale observation of hydrogen-induced, localized plastic deformation in fatigue-crack propagation in a pure iron. Scripta Mater 2017;140:13–7. https://doi.org/10.1016/j.scriptamat.2017.06.037.

[77] Ogawa Y, Birenis D, Matsunaga H, Takakuwa O, Yamabe J, Prytz Ø, Thøgersen A. The role of intergranular fracture on hydrogen-assisted fatigue crack propagation in pure iron at a low stress intensity range. Mater Sci Eng, A 2018;733:316–28. https://doi.org/10.1016/j.msea.2018.07.014.

[78] Birenis D, Ogawa Y, Matsunaga H, Takakuwa O, Yamabe J, Prytz Ø, Thøgersen A. Hydrogen-assisted crack propagation in α-iron during elasto-plastic fracture

toughness tests. Mater Sci Eng, A 2019;756:396–404. https://doi.org/10.1016/j.msea.2019.04.084.
[79] Ogawa Y, Umakoshi K, Nakamura M, Takakuwa O, Matsunaga H. Hydrogen-assisted, intergranular, fatigue crack-growth in ferritic iron: influences of hydrogen-gas pressure and temperature variation. Int J Fatig 2020;140:105806. https://doi.org/10.1016/j.ijfatigue.2020.105806.
[80] ASTM E647−13. Standard test method for measurement of fatigue crack growth rates. American Society for Testing and Materials; 2014. p. 1–50. https://doi.org/10.1520/E0647-13E01.2.
[81] Suresh S, Zamiski GF, Ritchie DRO. Oxide-induced crack closure: an explanation for near-threshold corrosion fatigue crack growth behavior. Metall Mater Trans 1981;12:1435–43. https://doi.org/10.1007/BF02643688.
[82] Slifka AJ, Drexler ES, Amaro RL, Lauria DS, Hayden LE, Stalheim DG, Chen Y. Summary of an ASME/dot project on measurements of fatigue crack growth rate of pipeline steels. In: American society of mechanical engineers, pressure vessels and piping division (publication) PVP. American Society of Mechanical Engineers (ASME); 2014. https://doi.org/10.1115/PVP2014-28938.
[83] Shinko T, Halm D, Benoit G, Hénaff G. Controlling factors and mechanisms of fatigue crack growth influenced by high pressure of gaseous hydrogen in a commercially pure iron. Theor Appl Fract Mech 2021;112. https://doi.org/10.1016/j.tafmec.2020.102885.
[84] Bilotta G, Arzaghi M, Hénaff G, Benoit G, Halm D. Hydrogen induced intergranular failure in armco iron under fatigue crack propagation. In: Volume 6B: materials and fabrication. ASME; 2016. https://doi.org/10.1115/PVP2016-63338. V06BT06A026.
[85] Grinberg NM. The effect of vacuum on fatigue crack growth. Int J Fatig 1982;4:83–95. https://doi.org/10.1016/0142-1123(82)90064-0.
[86] McEvily AJ, Gonzalez Velazquez JL. Fatigue crack tip deformation processes as influenced by the environment. Metall Trans A 1992;23:2211–21. https://doi.org/10.1007/BF02646014.
[87] Williams DP, Nelson HG. Embrittlement of 4130 steel by low-pressure gaseous hydrogen. Metall Trans A 1970;1:63–8. https://doi.org/10.1007/BF02819243.
[88] Smith P, Stewart AT. Effect of aqueous and hydrogen environments on fatigue crack growth in 2Ni-Cr-Mo-V rotor steel. Met Sci 1979;13:429–35. https://doi.org/10.1179/msc.1979.13.7.429.
[89] Gerberich WW, L1vne T, Chen XF, Kaczorowski M. Crack growth from internal hydrogen—temperature and microstructural effects in 4340 steel. Metall Trans A 1988;19:1319–34. https://doi.org/10.1007/BF02662593.
[90] Frandsen JD, Paton NE, Marcus HL. The influence of gaseous environments on fatigue crack growth in a nickel-copper alloy. Metall Trans A 1974;5:1655–61. https://doi.org/10.1007/BF02646339.
[91] James LA. Fatigue-crack propagation behavior of Inconel 718, NSA-33-007. 1975.
[92] Murakami Y, Kanezaki T, Mine Y, Matsuoka S. Hydrogen embrittlement mechanism in fatigue of austenitic stainless steels. Metall Mater Trans 2008;39:1327–39. https://doi.org/10.1007/s11661-008-9506-5.
[93] Onishi Y, Koyama M, Sasaki D, Noguchi H. Characteristic fatigue crack growth behavior of low carbon steel under low-pressure hydrogen gas atmosphere in an ultra-low frequency. ISIJ Int 2016;56:855–60. https://doi.org/10.2355/isijinternational.ISIJINT-2015-647.
[94] Sun Z, Moriconi C, Benoit G, Halm D, Henaff G. Fatigue crack growth under high pressure of gaseous hydrogen in a 15-5PH martensitic stainless steel: influence of pressure and loading frequency. Metall Mater Trans 2013;44:1320–30. https://doi.org/10.1007/s11661-012-1133-5.
[95] Wei R, Landes J. Correlation between sustained-load and fatigue crack growth in high-strength steels. Mater Res Stand 1969;9:25–46.
[96] Nibur KA, Somerday BP, San C, James M, Foulk W, Dadfarnia M, Sofronis P, Hayden GA. SANDIA REPORT Measurement and interpretation of threshold stress intensity factors for steels in high-pressure hydrogen gas. http://www.ntis.gov/help/ordermethods.asp?loc=7-4-0#online; 2010.
[97] Frandsen JD, Marcus HL. Environmentally assisted fatigue crack propagation in steel. Metall Trans A 1977;8:265–72. https://doi.org/10.1007/BF02661639.
[98] Komoda R, Yamada K, Kubota M, Ginet P, Barbier F, Furtado J, Prost L. The inhibitory effect of carbon monoxide contained in hydrogen gas environment on hydrogen-accelerated fatigue crack growth and its loading frequency dependency. Int J Hydrogen Energy 2019;44:29007–16. https://doi.org/10.1016/j.ijhydene.2019.09.146.
[99] Staykov A, Yamabe J, Somerday BP. Effect of hydrogen gas impurities on the hydrogen dissociation on iron surface. Int J Quant Chem 2014;114:626–35. https://doi.org/10.1002/qua.24633.
[100] Bulloch JH, Callagy AG. A detailed study of the relationship between fatigue crack growth rate and striation spacing in a range of low alloy ferritic steels. Eng Fail Anal 2010;17:168–78. https://doi.org/10.1016/j.engfailanal.2009.04.028.
[101] Cai H, McEvily AJ. On striations and fatigue crack growth in 1018 steel. Mater Sci Eng, A 2001;314:86–9. https://doi.org/10.1016/S0921-5093(00)01925-0.
[102] McEvily AJ, Matsunaga H. On fatigue striations. Sci Iran 2010;17:75–82. Transaction B: Mechanical Engineering.
[103] Pippan R, Zelger C, Gach E, Bichler C, Weinhandl H. On the mechanism of fatigue crack propagation in ductile metallic materials. Fatig Fract Eng Mater Struct 2011;34:1–16. https://doi.org/10.1111/j.1460-2695.2010.01484.x.
[104] Chen T, Chiba T, Koyama M, Akiyama E, Takai K. Factors distinguishing hydrogen-assisted intergranular and intergranular-like fractures in a tempered lath martensitic steel. Metall Mater Trans 2022;53:1645–58. https://doi.org/10.1007/s11661-022-06608-2.
[105] Kameda J, Mcmahon CJ. Solute segregation and hydrogen-induced intergranular fracture in an alloy steel. Metall Trans A 1983;14:903–11. https://doi.org/10.1007/BF02644295.
[106] Shibata A, Gutierrez-Urrutia I, Okada K, Miyamoto G, Madi Y, Besson J, Tsuzaki K. Relationship between mechanical response and microscopic crack propagation behavior of hydrogen-related intergranular fracture in as-quenched martensitic steel. Mater Sci Eng 2022;831:142288. https://doi.org/10.1016/j.msea.2021.142288.
[107] Novak P, Yuan R, Somerday BP, Sofronis P, Ritchie RO. A statistical, physical-based, micro-mechanical model of hydrogen-induced intergranular fracture in steel. J Mech Phys Solid 2010;58:206–26. https://doi.org/10.1016/j.jmps.2009.10.005.
[108] Nishikawa H, Oda Y, Noguchi H. Investigation of mechanism for intergranular fatigue crack propagation of low carbon steel JIS S10C in hydrogen gas environment. J Solid Mech Mater Eng 2011;5:263–78. https://doi.org/10.1299/jmmp.5.263.
[109] Martin ML, Fenske JA, Liu GS, Sofronis P, Robertson IM. On the formation and nature of quasi-cleavage fracture surfaces in hydrogen embrittled steels. Acta Mater 2011;59:1601–6. https://doi.org/10.1016/j.actamat.2010.11.024.
[110] Merson ED, Myagkikh PN, Poluyanov VA, Merson DL, Vinogradov A. Quasi-cleavage hydrogen-assisted cracking path investigation by fractographic and side surface observations. Eng Fract Mech 2019;214:177–93. https://doi.org/10.1016/j.engfracmech.2019.04.042.
[111] Homma T, Anata S, Onuki S, Takai K. Crack initiation and propagation behavior of hydrogen-induced quasi-cleavage fracture in X80 pipeline steel with stress concentration. Tetsu-To-Hagane/J IronSteel Instit Japan 2020;106:651–61. https://doi.org/10.2355/tetsutohagane.TETSU-2019-126.
[112] Dadfarnia M, Nagao A, Wang S, Martin ML, Somerday BP, Sofronis P. Recent advances on hydrogen embrittlement of structural materials. Int J Fract 2015;196:223–43. https://doi.org/10.1007/s10704-015-0068-4.
[113] Okada K, Shibata A, Takeda Y, Tsuji N. Crystallographic feature of hydrogen-related fracture in 2Mn-0.1C ferritic steel. Int J Hydrogen Energy 2018;43:11298–306. https://doi.org/10.1016/j.ijhydene.2018.05.011.
[114] Okada K, Shibata A, Matsumiya H, Tsuji N. Origin of serrated markings on the hydrogen related quasi-cleavage fracture in low-carbon steel with ferrite microstructure. ISIJ Int 2022;62. https://doi.org/10.2355/isijinternational.ISIJINT-2022-212. ISIJINT-2022-212.
[115] Vehoff H, Neumann P. Crack propagation and cleavage initiation in Fe-2.6%-Si single crystals under controlled plastic crack tip opening rate in various gaseous environments. Acta Metall 1980;28:265–72. https://doi.org/10.1016/0001-6160(80)90161-3.
[116] Nishikawa H, Oda Y, Noguchi H. Investigation of the mechanism for brittle-striation formation in low carbon steel fatigued in hydrogen gas (fractographic observation on fracture processes visualized by controlling load sequence and testing environment). J Solid Mech Mater Eng 2011;5:370–85. https://doi.org/10.1299/jmmp.5.370.
[117] Neumann P. New experiments concerning the slip processes at propagating fatigue cracks—I. Acta Metall 1974;22:1155–65. https://doi.org/10.1016/0001-6160(74)90071-6.
[118] Vehoff H, Neumann P. In situ sem experiments concerning the mechanism of ductile crack growth. Acta Metall 1979;27:915–20. https://doi.org/10.1016/0001-6160(79)90126-3.
[119] Oda Y, Furuya Y, Noguchi H, Higashida K. AFM and SEM observation on mechanism of fatigue crack growth in an Fe-Si single crystal. https://doi.org/10.1023/A:1014211617958; 2002.
[120] Andersson H, Persson C. In-situ SEM study of fatigue crack growth behaviour in IN718. Int J Fatig 2004;26:211–9. https://doi.org/10.1016/S0142-1123(03)00172-5.
[121] Shinko T, Hénaff G, Halm D, Benoit G. Influence of gaseous hydrogen on plastic strain in vicinity of fatigue crack tip in Armco pure iron. MATEC Web of Conferences 2018;165:03006. https://doi.org/10.1051/matecconf/201816503006.
[122] Nishikawa H, Oda Y, Takahashi Y, Noguchi H. Microscopic observation of the brittle-striation formation mechanism in low carbon steel fatigued in hydrogen gas (TEM and EBSD observation corresponding to fractography). J Solid Mech Mater Eng 2011;5:179–90. https://doi.org/10.1299/jmmp.5.179.
[123] Takahashi Y, Nishikawa H, Oda Y, Noguchi H. Microscopic characterization of hydrogen-induced quasi-brittle fatigue fracture in low-strength carbon steel. Mater Lett 2010;64:2416–9. https://doi.org/10.1016/j.matlet.2010.08.019.
[124] Awatani J, Katagiri K, Nakai H. Dislocation structures around propagating fatigue cracks in iron. Metall Trans A 1978;9:111–6. https://doi.org/10.1007/BF02647179.
[125] Awatani J, Shiraishi T. Dislocation structures adjacent to fatigue crack tips in stainless steel. Metall Trans A 1976;7:1599–601. https://doi.org/10.1007/BF02656408.
[126] Miller BD, Webb TW. Understanding the effect of crack tip deformation on fatigue crack growth behavior in 300-series austenitic stainless steel. Int J Fatig 2019;125:261–70. https://doi.org/10.1016/j.ijfatigue.2019.03.045.
[127] Katagiri K, Omura A, Koyanagi K, Awatani J, Shiraishi T, Kaneshiro H. Early stage crack tip dislocation morphology in fatigued copper. Metall Trans A 1977;8:1769–73. https://doi.org/10.1007/BF02646881.
[128] Purcell AH, Weertman J. Transmission electron microscopy of the crack tip region of fatigued copper single crystals. Metall Trans A 1973;4:349–53. https://doi.org/10.1007/BF02649636.
[129] Grosskreutz JC, Shaw GG. Fine subgrain structure adjacent to fatigue cracks. Acta Metall 1972;20:523–8. https://doi.org/10.1016/0001-6160(72)90008-9.
[130] Wilkins MA, Smith GG. Dislocation structures near a propagating fatigue crack in an Al/0.5%Mg alloy. Acta Metall 1970;18:1035–43. https://doi.org/10.1016/0001-6160(70)90059-3.

[131] Roven HJ, Nes E. Cyclic deformation of ferritic steel—II. Stage II crack propagation. Acta Metall Mater 1991;39:1735–54. https://doi.org/10.1016/0956-7151(91)90142-N.

[132] Roven HJ, Nes E. Cyclic deformation of ferritic steel—I. Stress-strain response and structure evolution. Acta Metall Mater 1991;39:1719–33. https://doi.org/10.1016/0956-7151(91)90141-M.

[133] Pham M-S, Holdsworth SR. Evolution of relationships between dislocation microstructures and internal stresses of AISI 316L during cyclic loading at 293 K and 573 K (20 °C and 300 °C). Metall Mater Trans 2014;45:738–51. https://doi.org/10.1007/s11661-013-1981-7.

[134] Mughrabi H, Christ H-J. Fatigue, cyclic deformation and microstructure. Cyclic deformation and fatigue of selected ferritic and austenitic steels: specific aspects. ISIJ Int 1997;37:1154–69. https://doi.org/10.2355/isijinternational.37.1154.

[135] Pham MS, Solenthaler C, Janssens KGF, Holdsworth SR. Dislocation structure evolution and its effects on cyclic deformation response of AISI 316L stainless steel. Mater Sci Eng, A 2011;528:3261–9. https://doi.org/10.1016/j.msea.2011.01.015.

[136] Birkbeck G, Inckle AE, Waldron GWJ. Aspects of Stage II fatigue crack propagation in low-carbon steel. J Mater Sci 1971;6:319–23. https://doi.org/10.1007/BF02403099.

[137] Kuhlmann-Wilsdorf D. Theory of plastic deformation: - properties of low energy dislocation structures. Mater Sci Eng, A 1989;113:1–41. https://doi.org/10.1016/0921-5093(89)90290-6.

[138] Kuhlmann-Wilsdorf D, Hansen N. Geometrically necessary, incidental and subgrain boundaries. Scripta Metall Mater 1991;25:1557–62. https://doi.org/10.1016/0956-716X(91)90451-6.

[139] Hansen N, Mehl RF, Medalist A. New discoveries in deformed metals. Metall Mater Trans 2001;32:2917–35. https://doi.org/10.1007/s11661-001-0167-x.

[140] Awatani J, Katagiri K, Shiraishi T. Microstructures around the tips of fatigue cracks growing at a low rate in iron. Metall Trans A 1976;7:807–10. https://doi.org/10.1007/BF02644077.

[141] Beachem CD. A new model for hydrogen-assisted cracking (hydrogen "embrittlement"). Metall Trans A 1972;3:441–55. https://doi.org/10.1007/BF02642048.

[142] Robertson IM, Sofronis P, Nagao A, Martin ML, Wang S, Gross DW, Nygren KE. Hydrogen embrittlement understood. Metall Mater Trans B 2015;46:1085–103. https://doi.org/10.1007/s11663-015-0325-y.

[143] Tabata T, Birnbaum HK. Direct observations of hydrogen enhanced crack propagation in iron. Scripta Metall 1984;18:231–6. https://doi.org/10.1016/0036-9748(84)90513-1.

[144] Vehoff H, Rothe W. Gaseous hydrogen embrittlement in FeSi- and Ni-single crystals. Acta Metall 1983;31:1781–93. https://doi.org/10.1016/0001-6160(83)90125-6.

[145] Chen X, Gerberich WW. The kinetics and micromechanics of hydrogen assisted cracking in Fe-3 pct Si single crystals. Metall Trans A 1991;22:59–70. https://doi.org/10.1007/BF03350949.

[146] Kimura A, Kimura H. Hydrogen embrittlement in high purity iron single crystals. Mater Sci Eng 1986;77:75–83. https://doi.org/10.1016/0025-5416(86)90355-1.

[147] Hinotani S, Ohmori Y, Terasaki F. Hydrogen crack initiation and propagation in pure iron single crystal. Mater Sci Technol 1994;10:141–8. https://doi.org/10.1179/mst.1994.10.2.141.

[148] Shibata A, Momotani Y, Murata T, Matsuoka T, Tsuboi M, Tsuji N. Microstructural and crystallographic features of hydrogen-related fracture in lath martensitic steels. Mater Sci Technol 2017;33:1524–32. https://doi.org/10.1080/02670836.2017.1312210.

[149] Cho L, Bradley PE, Lauria DS, Martin ML, Connolly MJ, Benzing JT, Seo EJ, Findley KO, Speer JG, Slifka AJ. Characteristics and mechanisms of hydrogen-induced quasi-cleavage fracture of lath martensitic steel. Acta Mater 2021;206:116635. https://doi.org/10.1016/j.actamat.2021.116635.

[150] Nakasato F, Bernstein IM. Crystallographic and fractographic studies of hydrogen-induced cracking in purified iron and iron- silicon alloys. Metall Trans A 1978;9:1317–26. https://doi.org/10.1007/BF02652256.

[151] Bernstein IM. Hydrogen-induced cracking in iron: morphology and crack path dependence. Metall Trans A 1970;1:3143–50. https://doi.org/10.1007/BF03038430.

[152] Troiano AR. The role of hydrogen and other interstitials in the mechanical behavior of metals. Metallograp Microstruct Analy 2016;5:557–69. https://doi.org/10.1007/s13632-016-0319-4.

[153] Yamaguchi M, Ebihara K-I, Itakura M, Kadoyoshi T, Suzudo T, Kaburaki H. First-Principles study on the grain boundary embrittlement of metals by solute segregation: Part II. Metal (Fe, Al, Cu)-Hydrogen (H) systems. Metall Mater Trans 2011;42:330–9. https://doi.org/10.1007/s11661-010-0380-6.

[154] Wang S, Martin ML, Robertson IM, Sofronis P. Effect of hydrogen environment on the separation of Fe grain boundaries. Acta Mater 2016;107:279–88. https://doi.org/10.1016/j.actamat.2016.01.067.

[155] Guzmán AA, Jeon J, Hartmaier A, Janisch R. Hydrogen embrittlement at cleavage planes and grain boundaries in bcc iron—revisiting the first-principles cohesive zone model. Materials 2020;13:5785. https://doi.org/10.3390/ma13245785.

[156] McEniry EJ, Hickel T, Neugebauer J. Ab initio simulation of hydrogen-induced decohesion in cementite-containing microstructures. Acta Mater 2018;150:53–8. https://doi.org/10.1016/j.actamat.2018.03.005.

[157] Tabata T, Birnbaum HK. Direct observations of the effect of hydrogen on the behavior of dislocations in iron. Scripta Metall 1983;17:947–50. https://doi.org/10.1016/0036-9748(83)90268-5.

[158] Robertson IM. The effect of hydrogen on dislocation dynamics. Eng Fract Mech 2001;68:671–92. https://doi.org/10.1016/S0013-7944(01)00011-X.

[159] Nagumo M, Takai K. The predominant role of strain-induced vacancies in hydrogen embrittlement of steels: overview. Acta Mater 2019;165:722–33. https://doi.org/10.1016/j.actamat.2018.12.013.

[160] Tateyama Y, Ohno T. Stability and clusterization of hydrogen-vacancy complexes in α−Fe : an ab initio study. Phys Rev B 2003;67:174105. https://doi.org/10.1103/PhysRevB.67.174105.

[161] Fukai Y. Formation of superabundant vacancies in M–H alloys and some of its consequences: a review. J Alloys Compd 2003;356–357:263–9. https://doi.org/10.1016/S0925-8388(02)01269-0.

[162] Sakaki K, Kawase T, Hirato M, Mizuno M, Araki H, Shirai Y, Nagumo M. The effect of hydrogen on vacancy generation in iron by plastic deformation. Scripta Mater 2006;55:1031–4. https://doi.org/10.1016/j.scriptamat.2006.08.030.

[163] Martin ML, Dadfarnia M, Nagao A, Wang S, Sofronis P. Enumeration of the hydrogen-enhanced localized plasticity mechanism for hydrogen embrittlement in structural materials. Acta Mater 2019;165:734–50. https://doi.org/10.1016/j.actamat.2018.12.014.

[164] Djukic MB, Bakic GM, Sijacki Zeravcic V, Sedmak A, Rajicic B. The synergistic action and interplay of hydrogen embrittlement mechanisms in steels and iron: localized plasticity and decohesion. Eng Fract Mech 2019;216:106528. https://doi.org/10.1016/j.engfracmech.2019.106528.

[165] Kacher J, Eftink BP, Cui B, Robertson IM. Dislocation interactions with grain boundaries. Curr Opin Solid State Mater Sci 2014;18:227–43. https://doi.org/10.1016/j.cossms.2014.05.004.

[166] Murr LE, Hecker SS. Quantitative evidence for dislocation emission from grain boundaries. Scripta Metall 1979;13:167–71. https://doi.org/10.1016/0036-9748(79)90286-2.

[167] Ono K, Meshii M. Hydrogen detrapping from grain boundaries and dislocations in high purity iron. Acta Metall Mater 1992;40:1357–64. https://doi.org/10.1016/0956-7151(92)90436-I.

[168] Chen Y-S, Lu H, Liang J, Rosenthal A, Liu H, Sneddon G, McCarroll I, Zhao Z, Li W, Guo A, Cairney JM. Observation of hydrogen trapping at dislocations, grain boundaries, and precipitates. Science 2020;367:171–5. https://doi.org/10.1126/science.aaz0122. 1979.

[169] Tien J, Thompson AW, Bernstein IM, Richards RJ. Hydrogen transport by dislocations. Metall Trans A 1976;7:821–9. https://doi.org/10.1007/BF02644079.

[170] Hwang C, Bernstein IM. Dislocation transport of hydrogen in iron single crystals. Acta Metall 1986;34:1001–10. https://doi.org/10.1016/0001-6160(86)90209-9.

[171] Wang S, Martin ML, Sofronis P, Ohnuki S, Hashimoto N, Robertson IM. Hydrogen-induced intergranular failure of iron. Acta Mater 2014;69:275–82. https://doi.org/10.1016/j.actamat.2014.01.060.

[172] Wan L, Geng WT, Ishii A, Du J-P, Mei Q, Ishikawa N, Kimizuka H, Ogata S. Hydrogen embrittlement controlled by reaction of dislocation with grain boundary in alpha-iron. Int J Plast 2019;112:206–19. https://doi.org/10.1016/j.ijplas.2018.08.013.

[173] Ding Y, Yu H, Lin M, Zhao K, Xiao S, Vinogradov A, Qiao L, Ortiz M, He J, Zhang Z. Hydrogen-enhanced grain boundary vacancy stockpiling causes transgranular to intergranular fracture transition. Acta Mater 2022;239. https://doi.org/10.1016/j.actamat.2022.118279.

[174] Ding Y, Yu H, Zhao K, Lin M, Xiao S, Ortiz M, He J, Zhang Z. Hydrogen-induced transgranular to intergranular fracture transition in bi-crystalline nickel. Scripta Mater 2021;204:114122. https://doi.org/10.1016/j.scriptamat.2021.114122.

[175] Neeraj T, Srinivasan R. Hydrogen embrittlement of steels : vacancy induced damage and nano-voiding mechanisms, vol. 73; 2017. p. 437–48.

[176] Shimokawa T, Tsuboi M. Atomic-scale intergranular crack-tip plasticity in tilt grain boundaries acting as an effective dislocation source. Acta Mater 2015;87:233–47. https://doi.org/10.1016/j.actamat.2015.01.002.

[177] Pokluda J, Siegl J. Mixed fatigue fracture morphology of ferritic ductile iron. Fatig Fract Eng Mater Struct 1990;13:375–85. https://doi.org/10.1111/j.1460-2695.1990.tb00608.x.

[178] Frandsen JD, Marcus HL. The correlation between grain size and plastic zone size for environmental hydrogen assisted fatigue crack propagation. Scripta Metall 1975. https://doi.org/10.1016/0036-9748(75)90285-9.

[179] Oriani RA. The diffusion and trapping of hydrogen in steel. Acta Metall 1970;18:147–57. https://doi.org/10.1016/0001-6160(70)90078-7.

[180] Quick NR, Johnson HH. Hydrogen and deuterium in iron, 49–506°C. Acta Metall 1978;26:903–7. https://doi.org/10.1016/0001-6160(78)90041-X.

[181] Pressouyre GM, Bernstein IM. A quantitative analysis of hydrogen trapping. Metall Trans A 1978;9:1571–80. https://doi.org/10.1007/BF02661939.

[182] Riku M, Matsumoto R, Taketomi S, Miyazaki N. Atomistic simulation study of cohesive energy of grain boundaries in alpha iron under gaseous hydrogen environment. J Soc Mater Sci Japan 2010;59:589–95. https://doi.org/10.2472/jsms.59.589.

[183] Matsuoka S, Tanaka H, Homma N, Murakami Y. Influence of hydrogen and frequency on fatigue crack growth behavior of Cr-Mo steel. Int J Fract 2011;168:101–12. https://doi.org/10.1007/s10704-010-9560-z.

[184] Laird C, Smith GC. Crack propagation in high stress fatigue. Phil Mag 1962;7:847–57. https://doi.org/10.1080/14786436208212674.

[185] Murakami Y, Matsuoka S. Effect of hydrogen on fatigue crack growth of metals. Eng Fract Mech 2010;77:1926–40. https://doi.org/10.1016/j.engfracmech.2010.04.012.

[186] Kanayama H, Ogino M, Miresmaeili R, Nakagawa T, Toda T. Hydrogen transport in a coupled elastoplastic-diffusion analysis near a blunting crack tip. J Computa Sci Technol 2008;2:499–510. https://doi.org/10.1299/jcst.2.499.

[187] Krom AHM, Koers RWJ, Bakker A. Hydrogen transport near a blunting crack tip. J Mech Phys Solid 1999;47:971–92. https://doi.org/10.1016/S0022-5096(98)00064-7.

[188] Kotake H, Matsumoto R, Taketomi S, Miyazaki N. Transient hydrogen diffusion analyses coupled with crack-tip plasticity under cyclic loading. Int J Pres Ves Pip 2008;85:540–9. https://doi.org/10.1016/j.ijpvp.2008.02.002.

[189] Matsuoka S, Yamabe J, Matsunaga H. Criteria for determining hydrogen compatibility and the mechanisms for hydrogen-assisted, surface crack growth in austenitic stainless steels. Eng Fract Mech 2016;153:103–27. https://doi.org/10.1016/j.engfracmech.2015.12.023.

[190] Higashida K, Tanaka M. Mechanism behind brittle-to-ductile transition understood by the interaction between a crack and dislocations. 2012.

[191] Taketomi S, Matsumoto R, Miyazaki N. Atomistic study of the competitive relationship between edge dislocation motion and hydrogen diffusion in alpha iron. J Mater Res 2011;26:1269–78. https://doi.org/10.1557/jmr.2011.106.

[192] Oriani RA, Josephic PH. Equilibrium aspects of hydrogen-induced cracking of steels. Acta Metall 1974;22:1065–74. https://doi.org/10.1016/0001-6160(74)90061-3.

[193] Wan D, Deng Y, Meling JIH, Alvaro A, Barnoush A. Hydrogen-enhanced fatigue crack growth in a single-edge notched tensile specimen under in-situ hydrogen charging inside an environmental scanning electron microscope. Acta Mater 2019;170:87–99. https://doi.org/10.1016/j.actamat.2019.03.032.

[194] Bilotta G, Henaff G, Halm D, Arzaghi M. Experimental measurement of out-of-plane displacement in crack propagation under gaseous hydrogen. Int J Hydrogen Energy 2017;42:10568–78. https://doi.org/10.1016/j.ijhydene.2017.02.084.

[195] Ogawa Y, Iwata K, Okazaki S, Nakamura M, Matsubara K, Takakuwa O, Matsunaga H. Fatigue crack-growth retardation after overloading in gaseous hydrogen: revisiting the effect of hydrogen on crack-tip plastic-zone development. Mater Lett 2022;308:131115. https://doi.org/10.1016/j.matlet.2021.131115.

[196] Kiuchi K, McLellan RB. The solubility and diffusivity of hydrogen in well-annealed and deformed iron. Acta Metall 1983;31:961–84. https://doi.org/10.1016/0001-6160(83)90192-X.

[197] Hagi H, Hayashi Y, Ohtani N. Diffusion coefficient of hydrogen in pure iron between 230 and 300 K. Transac Japan Institu Metals 1979;20:349–57. https://doi.org/10.2320/matertrans1960.20.349.

[198] Song J, Curtin WA. Mechanisms of hydrogen-enhanced localized plasticity: an atomistic study using α-Fe as a model system. Acta Mater 2014;68:61–9. https://doi.org/10.1016/j.actamat.2014.01.008.

[199] Itakura M, Kaburaki H, Yamaguchi M, Okita T. The effect of hydrogen atoms on the screw dislocation mobility in bcc iron: a first-principles study. Acta Mater 2013;61:6857–67. https://doi.org/10.1016/j.actamat.2013.07.064.

[200] Matsumoto R, Oyinbo ST, Vijendran M, Taketomi S. Hydrogen effect on the mobility of edge dislocation in α-iron: a long-timescale molecular dynamics simulation. ISIJ Int 2022;62. https://doi.org/10.2355/isijinternational.ISIJINT-2022-311. ISIJINT-2022-311.

[201] Katzarov IH, Pashov DL, Paxton AT. Hydrogen embrittlement I. Analysis of hydrogen-enhanced localized plasticity: effect of hydrogen on the velocity of screw dislocations in α-Fe. Phys Rev Mater 2017;1:033602. https://doi.org/10.1103/PhysRevMaterials.1.033602.

[202] Kapci MF, Yu P, Marian J, Liu G, Shen Y, Li Y, Bal B. Edge dislocation depinning from hydrogen atmosphere in α-iron. Scripta Mater 2024;247:116094. https://doi.org/10.1016/j.scriptamat.2024.116094.

[203] Hasan MS, Kapci MF, Bal B, Koyama M, Bayat H, Xu W. An atomistic study on the HELP mechanism of hydrogen embrittlement in pure metal Fe. Int J Hydrogen Energy 2024;57:60–8. https://doi.org/10.1016/j.ijhydene.2023.12.274.

[204] Nedelcu S, Kizler P. Molecular dynamics simulation of hydrogen-edge dislocation interaction in BCC iron. Phys Status Solidi 2002;193:26–34. https://doi.org/10.1002/1521-396X(200209)193:1<26::AID-PSSA26>3.0.CO;2-U.

[205] Taketomi S, Matsumoto R, Miyazaki N. Atomistic simulation of the effects of hydrogen on the mobility of edge dislocation in alpha iron. J Mater Sci 2008;43:1166–9. https://doi.org/10.1007/s10853-007-2364-5.

[206] Bhatia MA, Groh S, Solanki KN. Atomic-scale investigation of point defects and hydrogen-solute atmospheres on the edge dislocation mobility in alpha iron. J Appl Phys 2014;116. https://doi.org/10.1063/1.4892630.

[207] Kirchheim R. Solid solution softening and hardening by mobile solute atoms with special focus on hydrogen. Scripta Mater 2012;67:767–70. https://doi.org/10.1016/j.scriptamat.2012.07.022.

[208] Kimura H, Matsui H. Mechanism of hydrogen-induced softening and hardening in iron. Scripta Metall 1987;21:319–24. https://doi.org/10.1016/0036-9748(87)90221-3.

[209] Matsumoto R, Taketomi S. Molecular dynamics simulation of Surface-Adsorbed-Hydrogen-Induced Dislocation Motion in a thin film. Comput Mater Sci 2020;171:109240. https://doi.org/10.1016/j.commatsci.2019.109240.

[210] Deng Y, Barnoush A. Hydrogen embrittlement revealed via novel in situ fracture experiments using notched micro-cantilever specimens. Acta Mater 2018;142:236–47. https://doi.org/10.1016/j.actamat.2017.09.057.

[211] Takano N, Kidani K, Hattori Y, Terasaki F. Fracture surface of hydrogen embrittlement in iron single crystals. Scripta Metall Mater 1993;29:75–80. https://doi.org/10.1016/0956-716X(93)90257-S.

[212] Geng WT, Wang V, Li J-X, Ishikawa N, Kimizuka H, Tsuzaki K, Ogata S. Hydrogen trapping in carbon supersaturated α-iron and its decohesion effect in martensitic steel. 2018.

[213] Matsuoka S, Tsutsumi N, Murakami Y. Effects of hydrogen on fatigue crack growth and stretch zone of 0.08mass%C low carbon steel pipe. Transac Japan Soc Mechan Eng Series A 2008;74:1528–37. https://doi.org/10.1299/kikaia.74.1528.

[214] Narita N, Shiga T, Higashida K. Crack-impurity interactions and their role in the embrittlement of Fe alloy crystals charged with light elements. Mater Sci Eng, A 1994;176:203–9. https://doi.org/10.1016/0921-5093(94)90976-8.

[215] Taketomi S, Matsumoto R, Miyazaki N. Atomistic study of hydrogen distribution and diffusion around a {112}<111> edge dislocation in alpha iron. Acta Mater 2008;56:3761–9. https://doi.org/10.1016/j.actamat.2008.04.011.

[216] Cottrell AH. Dislocations and plastic flow in crystals. New York: Oxford Univ. Press; 1953.

[217] Lothe J. The effect of temperature on dislocations with condensed impurity atmospheres. Theory of dislocation motion and dislocation break-away. Acta Metall 1962;10:663–70. https://doi.org/10.1016/0001-6160(62)90133-5.

[218] Anderson PM, Hirth JP, Lothe J. Theory of dislocations. third ed. Cambridge University Press; 2017.

[219] Friedel J. Dislocations. first ed. Pergamon Press; 1964.

[220] Takakuwa O, Ogawa Y. Modeling hydrogen-assisted fatigue crack growth in low-carbon steel focusing on thermally activated hydrogen-dislocation interaction. Sci Technol Adv Mater 2025;26. https://doi.org/10.1080/14686996.2024.2436345.

[221] Merson E, Kudrya AV, Trachenko VA, Merson D, Danilov V, Vinogradov A. Quantitative characterization of cleavage and hydrogen-assisted quasi-cleavage fracture surfaces with the use of confocal laser scanning microscopy. Mater Sci Eng, A 2016;665:35–46. https://doi.org/10.1016/j.msea.2016.04.023.

[222] Anderson TL. Fracture mechanics fundamentals and applications. CRC Press; 2017.

[223] Chen X, Foecke T, Lii M, Katz Y, Gerberich WW. The role of stress state on hydrogen cracking in Fe-Si single crystals. Eng Fract Mech 1990;35:997–1017. https://doi.org/10.1016/0013-7944(90)90128-4.

[224] Cheng A, Chen N-Z. Fatigue crack growth modelling for pipeline carbon steels under gaseous hydrogen conditions. Int J Fatig 2017;96:152–61. https://doi.org/10.1016/j.ijfatigue.2016.11.029.